IMPLEMENTATION OF A COST EFFECTIVE NON-DESTRUCTIVE TESTING LABORATORY EXPERIMENT

by

Cameron F. Nye

A thesis submitted to the faculty of
The University of North Carolina at Charlotte
in partial fulfillment of the requirements
for the degree of Master of Science in
Applied Energy and Electromechanical Systems

Charlotte

2017

Approved by:

____
Dr. Wesley Williams

____
Dr. Stephen Kuyath

____
Dr. Aixi Zhou

ABSTRACT

CAMERON F. NYE. Implementation of a cost effective non-destructive testing laboratory experiment. (Under the direction of DR. WESLEY WILLIAMS)

A great amount of research is being performed in the field of Non-Destructive Testing (NDT). In addition, research is being performed in optimizing the distance learning experience, allowing students to gain equal involvement compared to students performing laboratory experiments on-campus. This research aims to address and combine both topics in creating a cost-effective Thermal NDT (TNDT) laboratory experiment intended for on-campus students as well as distance learning students. With NDT being used in industry, it is important for students to gain knowledge and experience related to this type of testing method.

This thesis details a laboratory trainer developed to be used to give students understanding of TNDT methods, both on campus and in remote laboratories. A sample specimen in the form of a 12” x 1/8”, x 3/4” bar stock is subjected to heat allowing the thermal response to be analyzed. Two samples are tested in total, one with a known defect, to determine which sample is ideal, and which is defective, using active TNDT techniques. Simulations and measured results are provided for comparison. The defect is carefully chosen so that students will have the opportunity to use multiple analytical techniques to choose which test subject contains the defect.

ACKNOWLEDGEMENTS

I would like to first thank my advisor Dr. Wesley Williams for approaching me about performing this research as well as his patience and constant availability. I have grown in many ways, both personally and professionally, under his direction. I would also like to thank Dr. Steve Kuyath and Dr. Aixi Zhou for their support and participation on my committee.

I would also like to thank the Department of Labor in partnership with the Mission Critical Operations consortium for making this research possible. I believe that their vision in enhancing the technical workforce is great and fully support their cause in furthering education in engineering.

I would like to lastly thank my parents, family, and friends for their constant support throughout this experience.

TABLE OF CONTENTS

LIST OF TABLES

LIST OF FIGURES

CHAPTER 1: INTRODUCTION

Remote control laboratories have been around since the early 90s [1] as an extension of industry protocols developed to control an automated process remotely. With the combination of remote control technology and the internet, cost-effective laboratory experiments can be developed to expose students to procedures that could not have been achieved prior [2]. Experiments offered remotely are now capable of introducing students to many new concepts that can be applied in industry [3]. Currently, there are many different types of remote laboratory experiments in varied subject areas that are offered to students. In addition to remote laboratories, hands on experiments are still very prevalent and advantageous as well at community colleges and universities [1]. With the research performed, an experiment will be created to achieve a hybrid exercise that can be performed hands-on or remotely through a virtual server.

The experiment created will focus around Non-Destructive Testing (NDT), specifically Thermal NDT (TNDT). NDT is a form of testing used in industry to evaluate structural or mechanical components' condition in a way that doesn't ruin their integrity [4]. Examples of components could include: circuit boards, motors, and pipelines. There are many different types of NDT methods including: Visual and Optical Testing (VT), Radiography

(RT), and Ultrasonic Testing (UT), Magnetic Particle Testing (MT), and Penetrant Testing (PT) [4]. Another important concept of many laboratory experiments is background code that may not be seen on the front end that performs tasks the student may not be responsible

for, including: image processing, data acquisition, and algorithm-based computations. For this reason, scripts were required in creating this experiment to handle these types of functions. Multiple software platforms were used including: Raspbian terminal (Raspberry Pi), MATLAB R016a, LabVIEW, and Simulink. When introducing the background code, two parts will be described. Part 1 will consist of the experimental test script while Part 2 will focus on image processing scripting.

The first part is implemented using a Raspberry Pi and uses modified code to capture a thermal image. A master script was written so that, once executed, energizes a relay triggering a heater that applies heat to the test subject. A separate process starts in parallel that captures thermal images at specified time intervals. The second part of the process focuses on translating the images into a usable format that students can easily view and decide if a test subject is defective or not. MATLAB and Simulink were used as the software platforms to handle all image processing. A high-level flow chart of the two processes combined may be seen below.

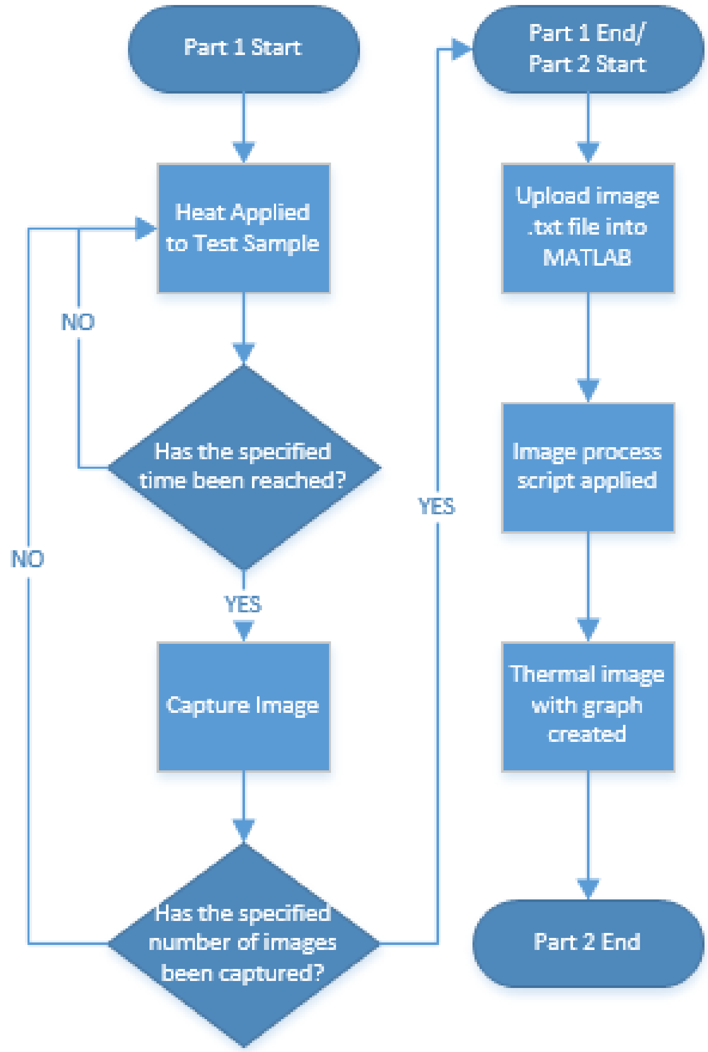

Figure 1: High level flowchart depicting the process of acquiring an image and apply image processing

CHAPTER 2: LITERATURE REVIEW

2.1 THERMAL NON-DESTRUCTIVE TESTING

Non-Destructive Testing (NDT) plays an important role in modern day industry practices saving both time and money. TNDT gives industrial manufacturers a viable option to test pieces of machinery and equipment for defects or anything that would compromise the integrity of equipment. For this reason, a hybrid laboratory experiment giving on-campus and distance education students an opportunity to be exposed to these concepts is necessary.The roots of thermal NDT can be traced back to 1770 when Pictet, a French scientist [5]. In Pictet's experiment, he focused on the concentration of heat by curved mirrors. In the early 1900s, Einstein, Golitzyn, Kirchoff, Planck, Wien et al. discovered the laws of thermal radiation [5]. It wasn't until the 1960s, however, that Infrared (IR) thermography began seeing practical uses in thermal testing applications thanks to radiometric IR imagers from AGA, Sweden (now FLIR Systems, USA) [5]. Furthering TNDT can be attributed by Vavilov et al., Carlomagno and Terardi, Vavilov and Taylor, MacLaughlin and Mirchandani, Balageas et al., Mandelis, and other authors who introduced one-dimensional, two-dimensional, and three-dimensional models of defects [5]. Today, IR diagnostics continue to improve due to increasing technology in IR technology and data processing.To understand a sample undergoing TNDT, the following model may be used.

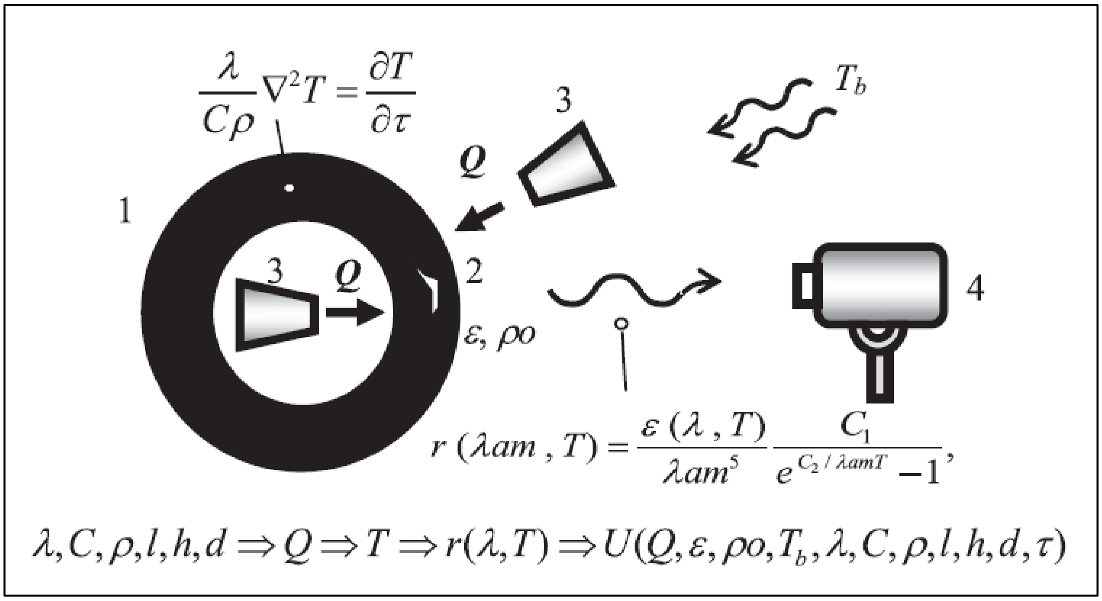

Figure 2: TNDT basic model [12]

1 = Test Sample

2 = Defect

3 = Thermal Stimulation Source

4 = IR Imager

Q = heat flux

Λ = material thermal conductivity

ε = material emissivity

po = reflectivity

C = specific heat capacity

p = density

l = defect depth

h = lateral size

d = thickness

T = temperature

Tb = Background reflected temperature

In this sample model, the thermal stimulation of any physical nature is described. The transient heat flux, *Q*, due to heat diffusion depends on multiple model parameters relating to material quality [5]. From this, the following data processing algorithm may be used.

$$\Delta T(x, y, \tau) = T(x, y, \tau) - T_{ref}(x, y, \tau) \quad (1)$$

In this equation, $T(x, y, \tau)$ is a sample temperature taken at a specific coordinate at time, τ. In comparison, $T_{ref}(x, y, \tau)$ is the reference temperature of a non-defective object at the same coordinate taken at time, τ. The result, $\Delta T(x, y, \tau)$, represents the temperature differential between the two test samples.

There are various TNDT techniques available today. Two popular versions of TNDT techniques include active and passive thermography. The passive approach may be described as an approach used when there is a noticeable contrast between the test sample and ambient temperature. This allows an IR to capture the contrast to detect any defects in a TNDT application .

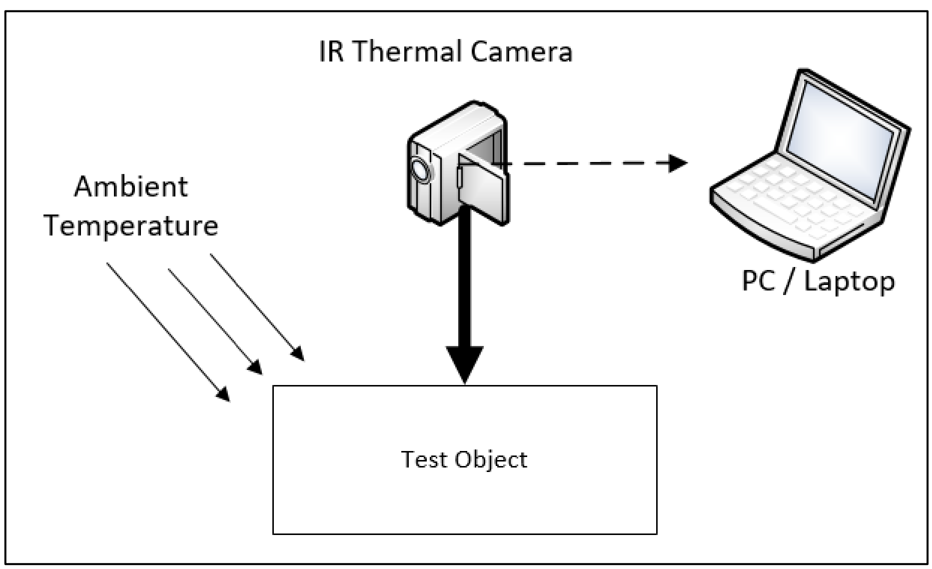

Figure 3: TNDT: Passive thermography

Simple applications of passive TNDT may include outdoor testing of electrical components on transmission lines (Left) or indoor testing of heavy machinery components such as motors (Right).

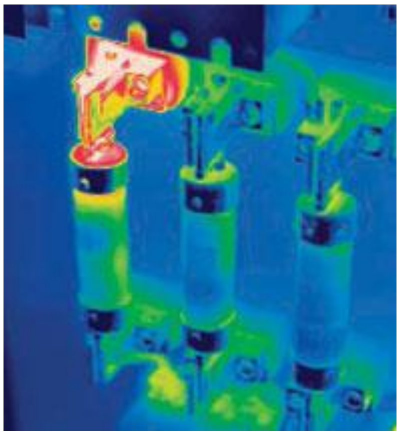

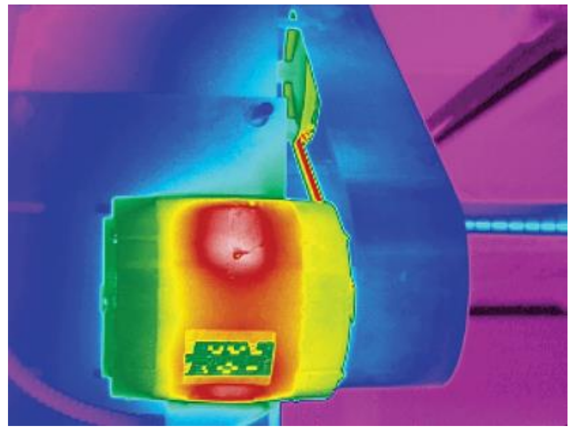

Figure 4: TNDT Testing: Thermal image of transmission components (LEFT); Thermal image of motor (RIGHT)

Active thermography may be described where an external heating or cooling source is used to introduce heat or cooling to the test sample [5]. Using this method, the sample is excited with an external source and its thermal response captured using an IR camera. This method is useful when detecting internal defects that may not be detected with visual inspection. The heating or cooling source may be applied directly or indirectly creating a contrast in temperatures to be recorded by an IR camera. A basic active TNDT setup can be seen below. In this example, a heating/cooling source is applied directly to the test object.

2.2 REMOTE LABORATORY EXPERIMENT APPLICATIONS

There have been many attempts to improve the distance learning experience including the development of remote laboratory experiments. Remote laboratory experiments have many applications advantageous to students and allow students to access the lab experiments at their convenience.

Alhalabi, Hamza, and Humos [3] found that a Remote Labs Environment (RLE) was accepted widely to a variety of students from different colleges, different majors, and different educational levels. The purpose of their experiment was to determine which type of learning method was preferred for laboratory experiments between the following: RLE (or RL), Software Simulation (SS) and against Campus Labs (CL). Two experiments were performed: 1. Active Element (Transistor) Characterization Experiment and 2. Measuring Static and Kinetic Friction on an Inclined Plane. From these experiments, 50% of the students found RLE to be more realistic than SS while 28% believed SS experiments were more realistic than RLE. Also, 31% preferred RLE type learning experiments than CL and SS although 57% preferred CL [3].

Brock J. LaMeres, an assistant professor in the electrical and computer engineering department at Montana State University, and Carolyn Plumb, the Director of Educational Innovation and Strategic Projects at Montana State University, researched the differences in learning from hands-on experiments to remote experiments on students enrolled in a class related to microprocessor hardware and software systems. Lameres and Plumb measured the level of understanding using five different learning categories [6]:

1. Basic architecture of a stored-program computer
2. Addressing modes of a microprocessor
3. Typical I/O interface and understanding timing
4. Analyzing the interaction between the microprocessor and memory with a timing diagram
5. Synthesize a timing diagram of a given read/write cycle between the microprocessor and memory

These five categories were assessed by conducting self-surveys, weighted multiple choice questions, and short answer questions [6]. A total of ten different experiments were performed throughout the course that covered the five learning categories. Three different groups were tested including: control, hands-on only, and remote access only. The control group consisted of students enrolled in a class focused on microprocessor hardware and software systems. The two groups: hands-on and remote access, were students enrolled in the same class a year later but only allowed to perform the experiments hands-on or through remote access [6]. The surveys consisted of a pre-assessment and post-assessment of the student's understanding. The sample size of each group can be seen below:

Table 1: Survey results from student's experience with hands-on and remote access laboratory experiments [6]

	Control		**Hands-On**		**Remote Access**	
	Pre	Post	Pre	Post	Pre	Post
	N = 46	N = 41	N = 32	N = 30	N = 15	N = 14
Outcome 1 Question	6.304	7.293	6.563	7.600	5.627	6.143
Outcome 2 Question	6.891	8.634	6.625	8.300	5.600	7.786
Outcome 3 Question	5.283	6.683	5.844	6.767	3.867	5.429
Outcome 4 Question	6.152	7.512	6.688	7.767	5.067	7.071
Outcome 5 Question	5.587	6.805	6.031	7.300	4.400	6.429

In conclusion of this experiment, the level of understanding of the five categories by students exposed to remote access only experiments did not differ drastically from those in the control group and hands-on group [6].

This technology has been, and is presently being, explored so that many different application experiments can be offered to end users as learning tools. Colak and Efe [7] explore a specific application using a Programmable Logic Controller (PLC) training set. In their system, a SIEMENS S7-200 PLC was used in order to control an induction motor. The programming software Simatic Step 7 was used in order to control the ladder logic programming. The hardware used in this experiment was a SIEMENS PLC, frequency converter, induction motor, and encoder. Students were able to login to a server-based reservation from the internet. From there, students could study theoretical information and modify the pre-programmed example ladder logic program offered. Although this specific example doesn't offer the freedom of a truly hands-on experiment, the underlying concepts could be learned and applied to real-world applications involving PLCs similar to this model using ladder logic software.

Another example of this technology being implemented includes the implementation of an elevator application being controlled remotely by a National Instruments (NI) myRIO and an Allen Bradley Micro 800 series PLC [8]. This application focuses on the hybrid control of an elevator with 2 separate shafts. The system is comprised of motors, sensors, and actuators, all of which can be controlled by a student. Students could make a reservation to a virtual machine to create and execute code. A server was used in order to manage each student account and reservation. An important feature of this application included safety features that provided maximum limits for linear travel controlled by each motor. In total, there were three controllers present on the trainer system. There were two NI myRIO microcontrollers and one Allen Bradley Micro 800 Series PLC. The purpose of having three controllers was to provide students with the opportunity of controlling the process of an elevator using NI LabVIEW software or Rockwell Automation's ladder logic software Connected Components Workbench (CCW). One NI myRIO and the PLC were available for students to program while the second NI myRIO acted as a supervisory controller which monitored each input. If a student were to program the device to perform an action outside of the system's boundaries the supervisory controller would reject this request to maintain system integrity.

A different approach to the same hybrid control architecture is the implementation of a cartesian robot with multiple degrees of freedom [9]. This application applies the same concepts used with the implementation of the elevator trainer and adds multiple degrees of freedom increasing the complexity of the system. Following the same control architecture described in the previous elevator trainer example, two NI myRIOs and an Allen Bradley Micro800 series PLC were used to give students the opportunity to program this system in multiple languages. The cartesian robot is a four degree of freedom (DOF) system allowing control over three separate axes: X, Y, and Z. An application currently implemented involves a platform containing golf balls. A sample experiment may require the user to move the golf balls to a certain location on the platform. An important concept about this system, which should be taken into consideration for any RLE exercise, is a resettable option. For this system, a student may make mistakes and would need to reset the system to go to a known location and to clear the platform free of golf balls to start over. Another important aspect involving the resettable feature is when a student ends his/her reservation the system must perform a reset to clear the platform of golf balls and move each axis to a known starting location. A server was used for this system as well to manage student account permissions and reservations.

2.3 THERMOGRAPHY / NDT APPLICATIONS

Clark, McCann, and Forde studied the application of IR thermography to the non-destructive testing of concrete and masonry bridges [10]. Clark, McCann, and Forde used the concept of IR energy that states: any object with a temperature above absolute zero emits IR energy, to monitor the integrity of concrete and masonry bridges. Faults to concrete structures that have been detected by IR technology include cracks and delaminations. In this research experiment, two separate bridges were tested. It was noted that, when using IR testing outdoors, careful consideration to the weather must be taken into consideration. The sun or wind both have the potential to change the surface temperature of an object as well as the conductivity and emissivity, which both play an important role in capturing the accurate IR energy. Using an Agema Thermovision 900 Camera, multiple images were captured at each bridge. After processing these images using imaging software, the determination was made that each site had potential wet spots and delaminations that will degrade the integrity of the bridges.

Swiderski and Vavilov also explored the use of TNDT by using this technology for detecting defects in multi-layered composite materials used in military applications [7]. Composite materials are being used more and more with the construction of light ballistic operations. Composites may be applied to textile materials joined with plastic to create a multi-layered composite material used for personal ballistic protection devices such as helmets and vests. A common defect found in the process of combining each composite layer is the inaccuracy of the amount of glue applied to each layer. This may lead to failures in the form of delaminations on layers occurring under hits of fragments and bullets. Swiderski and Vavilov tested a seven-layer subject consisting of four layers of polyaramide joined with a formaldehyde resin glue (3 layers). For the experiment, an AGEMA 900 IR LW camera was used for capturing the thermal images. A heating lamp was used as the heat source and positioned 0.5m from the sample. It was concluded that for this specific application, TNDT is not the best method for finding defects. From computer simulations, it was determined that, although TNDT is not the best method for this application, defects in the upper layers of the composite could be identified.

Research performed by: J.A. Schroeder, T. Ahmed, B. Chaudhry, and S. Shepard [11] uses the concepts of thermography NDT and applies them by testing structural composites and adhesively bonded composite joints. DaimlerChrysler, Ford, and General Motors formed a partnership with the automotive composites consortium (ACCS) to focus on the use of structural adhesive bonding as an important enabling technology used for the assembly of large composite pieces. To verify quality assurance, a method of NDT was needed. Pulsed thermography was chosen as the method of thermographic NDT because this method offered the best overall performance for detecting typical defects found in the composite and adhesive bond, inspection speed, and automation potential [11]. After testing this method on a truck bed with multiple adhesive bonds, this method proved to be effective at validating the quality of the bond. The focal point of this test subject was the bonded cross-sills. The quality of the bonding of the cross-sills to the truck bed itself were examined and tested for quality assurance. The equipment used to perform the test was an EchoTherm32 NDT System [11]. This system could capture 12-bit data continuously at a 60 Hz frame rate for 30s after heat pulses were applied to the test sample. Large parts were divided into smaller sections due to the field of view of the EchoTherm32. The picture at 23 seconds can be seen to display the composite bond between the cross-sill and the truck bed. Also, a lighter shade seen within the bond can be seen. This was described to be a disbond and would require maintenance. This does, however, proves that IR thermography is a promising technology that can be applied to automotive quality assurance testing.

In 2013, N.P. Avdelidis, C. Ibarra-Castanedo, X.P.V. Maldague [12] used a form of thermography NDT to inspect glass reinforced plastic (GRP) wind turbine blades. Specifically, pulsed thermography was used to evaluate the GRP wind turbine blades structurally. The turbine blades tested were GRP blades using an epoxy based resin composite. Early detection of damage to the composite structure is essential to prevent further damage. For testing, because the thermal conductivity of each test sample was relatively low, samples were tested using a reasonably low maximum frame rate [12]. The heat source was provided by a heat lamp. The lamp provided a uniform heat to the surface at a relative short pulse of a few milliseconds. The tests were validated by viewing samples at different frequencies to verify the integrity of the bond in the GPR blade.

Another TNDT application example was explored in 2013 by: Liu Chengyan, Qin Fei, and Ban Zhaowei, from Beijing University of Technology [10], in which the application of IR Thermography being used to detect defects in electronic packages. Defects such as: delaminations, cracks, and voids contribute to the weakness of the structure upon fabrication. The demand for such defects has increased recently due to the growing number of non-destructive testing methods that can efficiently localize defects with high detection sensitivity. For this application, multiple non-contact methods were evaluated but IR Thermography was chosen because of the following characteristics: non-contact, real-time recording, and rapidity. Several experimental samples containing a variety of defects related to the copper and molding compound of the electronic packages were tested. Specifically, a series of samples containing different defect sizes were investigated. The samples were prepared using mold compound and copper, which were adhesive with thermal glue. Although the dimensions of the entire package were not given, one of the defects within a sample had a diameter of 5mm, a thickness of 1.5mm and a depth of 1.5mm indicating, with the right equipment, small defects could be detected. It was noted that samples with defects at greater depths could be detected, but not with the same detection sensitivity as those with a smaller depth.

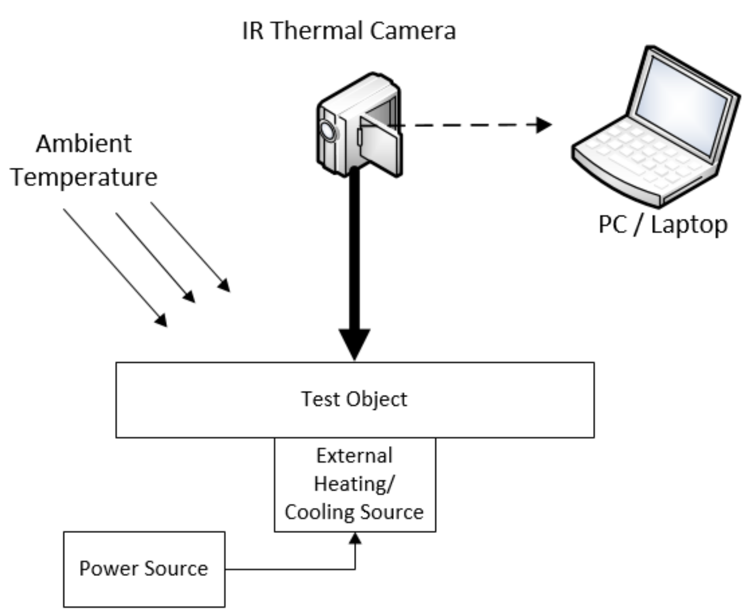

Figure 5: Active thermography

An example application of active TNDT may be seen below. In this example, pulsed thermography, an active TNDT method, was used to detect any possible delaminations in automobile manufacturing.

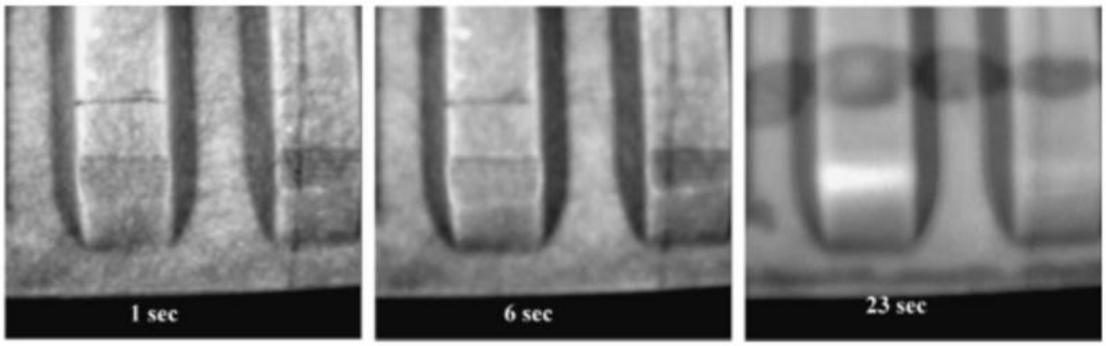

Figure 6: TNDT test performed by pulsed thermography verifying bonding techniques used in the automotive industry

CHAPTER 3: EXPERIMENTAL DESIGN

In this chapter, the experimental design is described in detail. An overview of the selection process of the components used will be given. The methods in which these components are applied will be described to give a better understanding of how this experiment will effectively introduce students to TNDT with a low cost experiment that is adaptable to remote laboratory experiments..

3.1 EXPERIMENTAL OVERVIEW

The goal of this experiment is to introduce students to an academic version of TNDT. As previously noted, IR thermography can be broken down into two main methods described above: Active and Passive [13]. By definition, this experiment uses the active TNDT method.

The basic construction of the experiment consists of an aluminum frame that holds a test subject, in this case, bar stock that measures 12” x $^{1}/_{8}$” x $^{3}/_{4}$”. A heat source, measuring 1” x 2” was applied directly in the middle of the test subject. When heat is applied, a thermal camera captures images at specific time intervals monitoring the rate of temperature change and heat transfer throughout the sample. In the process of capturing a thermal image, a temperature conversion formula is applied to each image pixel that converts raw pixel data into a temperature (°C) data. This allows students to diagnose the condition of the test subject with the use of a thermal image and temperature graph.

3.2 COMPONENT SELECTION

The main component for the construction of the experiment was the thermal camera being used. For this experiment setup, a cost-effective camera was preferred so a 60x80 pixel FLIR Lepton thermal imaging module was selected. The FLIR Lepton imaging module consists of a microbolometer sensor array to capture Long-Wave Infrared (LWIR) signals (8μm - 14μm). When capturing images, the emissivity is assumed to be 1 (an ideal blackbody). The camera has built-in signal-processing electronics that are intended to make system integration straight-forward [14]. The camera was purchased with a development board to insert the camera module into. A visual reference of the module and development board can be seen below:

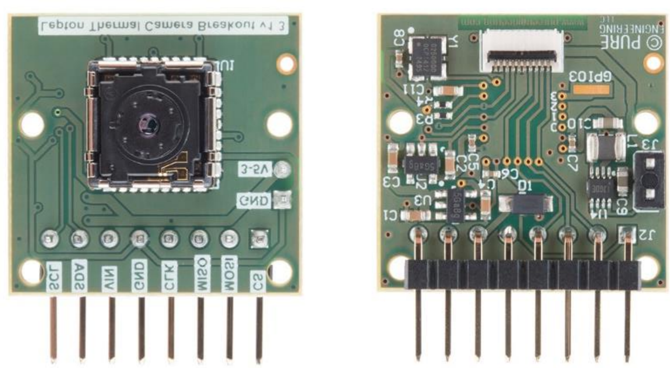

Figure 7: FLIR Lepton development kit: camera and development board

With the development board, the necessary connections of the camera module were routed to male pins. A datasheet containing important specifications may be referenced in Appendix A.

To integrate the camera into the project, the camera needed to be connected to a microcontroller to receive images being captured. The microcontroller selected was a Raspberry Pi 3. Multiple microcontrollers were evaluated and the Raspberry Pi was chosen based on processing power, digital I/O, available onboard communication protocols, as well as sample code being offered. The sample code offered a strong foundation to capture raw pixel data from the camera to be processed. The Raspberry Pi is a Linux based system with multiple USB ports, an HDMI port, and audio port. A monitor, keyboard, and mouse can all be connected to the Raspberry Pi. The operating system (OS) used is Raspbian. Using Raspbian, different .c files and scripts could be created and executed in the terminal window. All of these capabilities made the Raspberry Pi the ideal choice to integrate the FLIR Lepton thermal imaging system to.

Another important component to this project was the heating source applied to the test subject. Multiple heaters were evaluated and a silicone rubber fiberglass insulated heater was chosen from the manufacturer Omega. A drawing of the heater selected can be seen below.

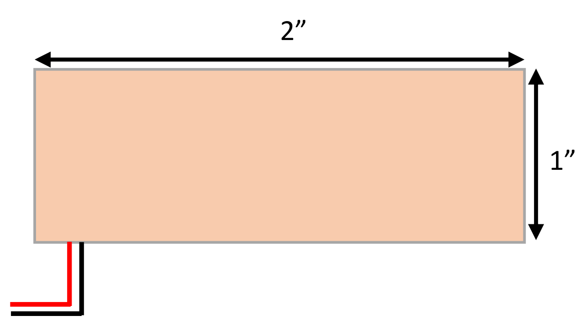

Figure 8: Omega silicone rubber fiberglass insulated flexible heating pad dimensions

This specific heater was chosen because of its heating temperature range and favorable dimensions. The maximum safe operating temperature that could be achieved with this type of heater is 232°C so the desired temperature of ≈70°C could be reached. However, to achieve a constant value of ≈70°C, a pulse-width modulated (PWM) signal was used and implemented by a solid-state relay (SSR). Specific specifications of the heater may be referenced in Appendix B.

The relay selected was a solid-state zero-cross relay that provided 120V triggered from an output of the Raspberry Pi. A zero-cross relay, or synchronous, relay is the most common type of SSR used today. Further specifications may be referenced in Appendix C. The PWM signal was a high frequency switching signal so a solid-state relay was used to avoid any signal delay an electromechanical relay may cause. Also, solid-state relays consume less power making it a better option being powered from the low current sourcing outputs of the Raspberry Pi. Another advantage of the zero-crossing SSR is that, when triggered, the switching occurs at the zero-crossing point of the AC sine-wave reducing load current through the load [15]. The relay has a documented a minimum threshold voltage of 3.3V, however upon testing 5V was needed. A diagram of the relay circuit may be viewed below.

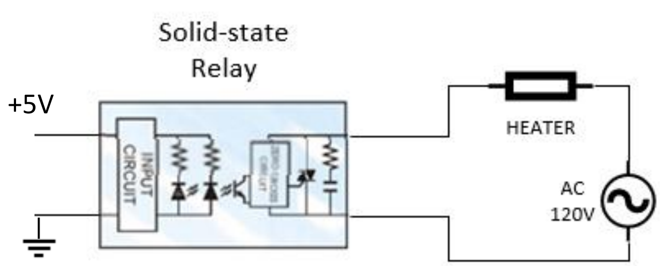

Figure 9: Solid-state relay circuit used to modulate power to the heating pad

All the components listed above were combined to create the cost-effective laboratory experiment package. A sub-circuit was added to step up the voltage from the output of the Raspberry Pi to meet the threshold voltage of the relay. A complete circuit diagram of the experiment is pictured below.

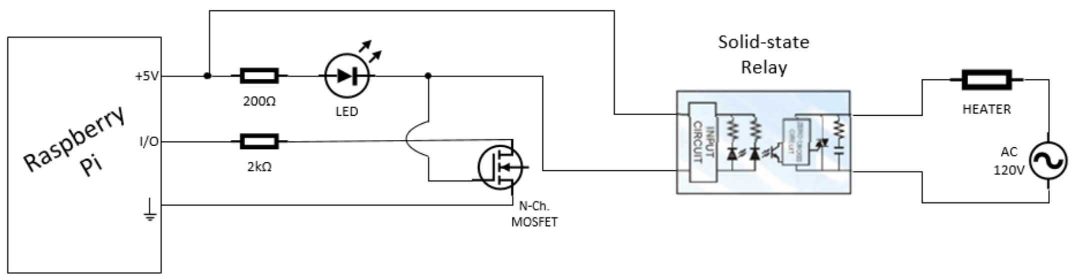

Figure 10: Overall experiment circuit layout

3.3 CALIBRATION

As stated earlier, example code for capturing an image using the FLIR Lepton thermal imaging module was provided from the purchase site [16]. Using this code, however, only resulted in a gray-scale thermal image, auto-scaled best on the maximum and minimum temperatures. To convert each pixel into a usable temperature measurement, additional steps were necessary. A new temperature conversion formula needed to be applied to each pixel element of an image converting raw pixel values into useful temperature values that could be analyzed by the student. Research performed resulted in three equations that have been used in previous unrelated applications to complete this task. Each equation may be seen below.

$$\left(\left((0.05872x) - 479.23 + 75\right) - 32\right) * \frac{5}{9} \tag{2}$$

$$0.0217x + 23.8 - 177 \tag{3}$$

$$0.0465x - 349.44 \tag{4}$$

Each of these equations were generated using various calibration methods over various temperature ranges. In addition to these calibration equations, two additional equations were calculated by a calibration method consisting of setting the camera in front of a heating pad and capturing raw pixel data over a temperature range from 21.8°C to 52.1°C. A heating pad was used as the temperature source to relate each raw pixel value to a temperature value. Over a period of time, the heat source increased while an image was captured at various time intervals. The raw pixel values were then associated to the temperature of the heat source at the time an image was captured. The known heat value of the heating pad was measured using a non-contact laser broadband IR pyrometer. The temperature range of this specific IR laser pyrometer was between the range of -50°C - 80°C. The comparison between the data collected from the camera and the IR laser pyrometer can be analyzed using Wien's displacement law:

$$\lambda_{max} = \frac{b}{T} \tag{5}$$

Where, b is Wien's displacement constant and is equal to 2.89773*cm*K (≈2900μm*K) and T is temperature in Kelvin, and λ_{max} is the IR wavelength measured. Using this equation, the wavelength range can be calculated by substituting the minimum and maximum temperatures the laser pyrometer is capable of measuring. In doing this, the accurate wavelength range can be calculated to be between 8μm to 13μm. Comparing this range to that of the FLIR Lepton (8μm to 14μm), it was determined that this laser pyrometer was sufficient for temperature calibration. Once verified, the temperature was increased on the heating pad while images were captured using the FLIR camera.

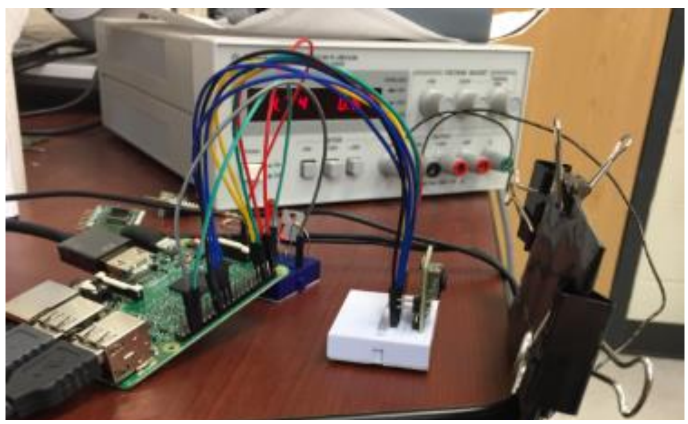

Figure 11: FLIR Lepton camera calibration setup

The heating pad used was constructed of a mesh of polyester filament and micro metal conductive fiber folded into a protective polyimide film. Aluminum was placed over the heating pad to evenly distribute the heat. In addition, tape was placed over the aluminum to reduce the reflective properties of the aluminum that would otherwise cause inaccurate data. The results of the calibration may be seen below.

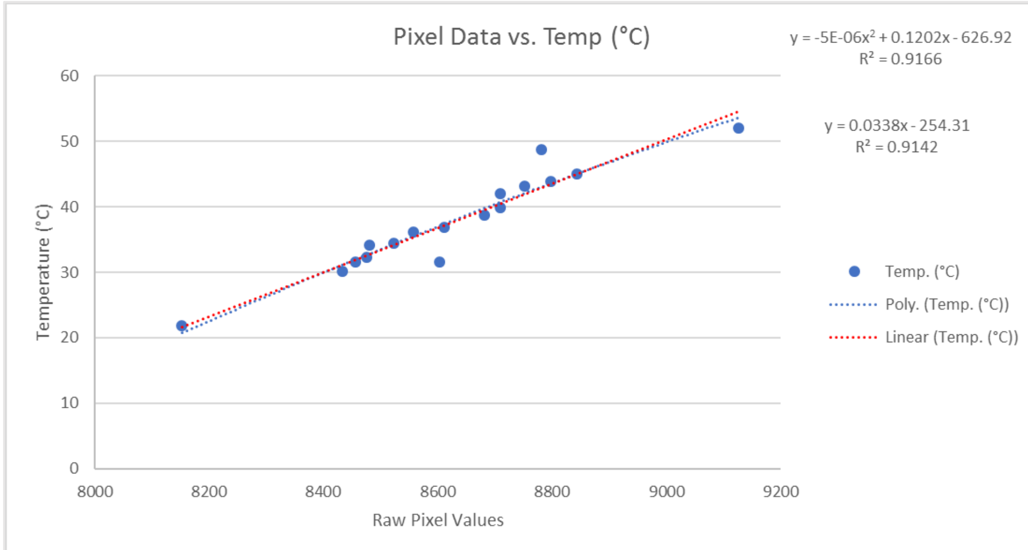

Figure 12: Temperature correlation to raw pixel data value; linear and polynomial best-fit equations applied

Two additional temperature conversion equations were generated using this calibration method. One linear equation and one polynomial equation, which may be seen below.

$$0.0338x - 254.31 \tag{6}$$

$$-5 \cdot 10^{-6}x^2 + 0.1202x - 626.92 \tag{7}$$

Once these equations were obtained, further testing was performed to verify the accuracy of each. According to the FLIR Lepton datasheet (Appendix A), the module requires a minimum distance of 4” from the camera to acquire accurate pixel data. When testing each temperature conversion equation, images were captured at a distance of 6”, 12”, and 18” from the camera. Temperatures were measured at 24 different locations on the hand to compare to the temperature values acquired from each temperature conversion method. A visual reference of this calibration technique may be referenced below.

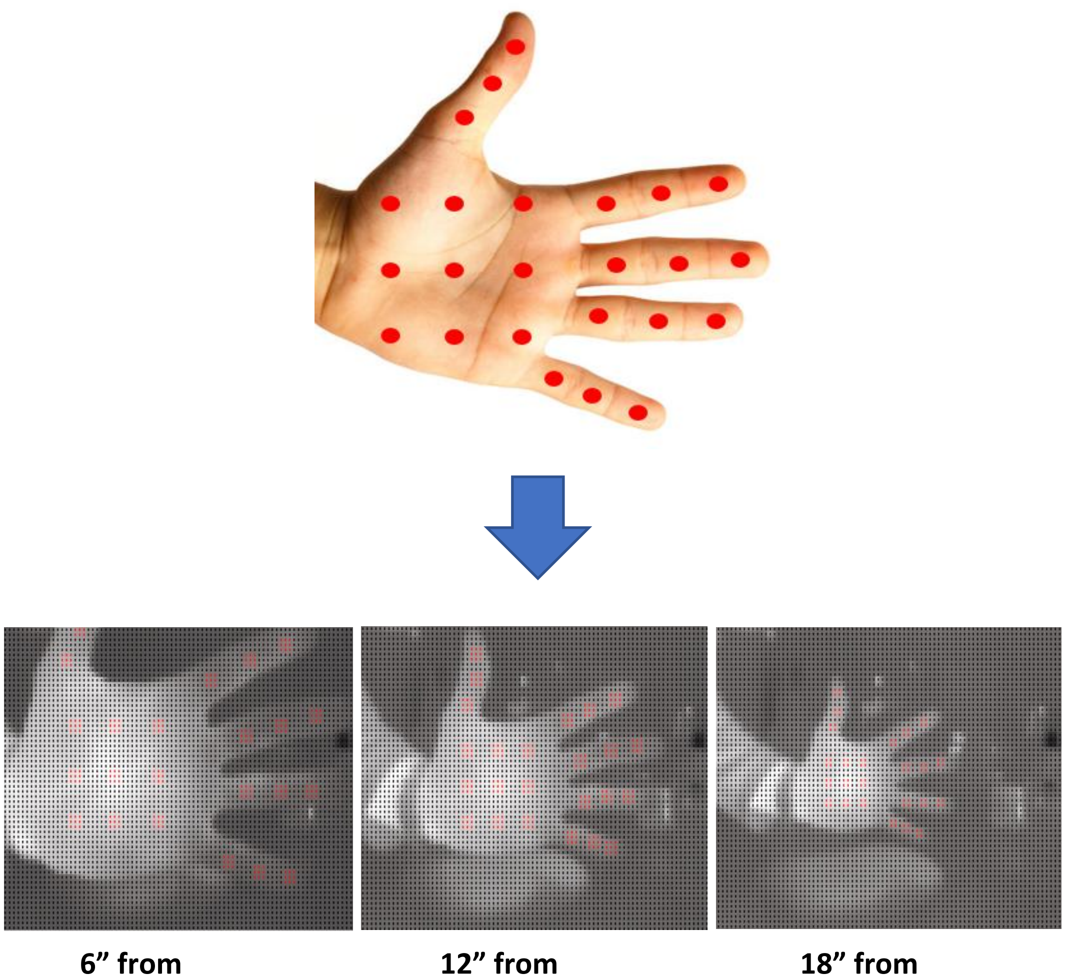

Figure 13: Test points measured and compared to images at 6” (LEFT), 12” (MIDDLE), and 18” (RIGHT)

To obtain images with raw pixel data, the example code provided was modified and executed using Raspbian terminal window. By executing the code, a .txt file with raw pixel data was obtained. This data was then transferred to Excel for further analysis. For each image, the equation was applied to each individual pixel to convert raw pixel data to temperature (°C) values. All five equations were evaluated and tested to see which had the lowest % Error. The equation used to test each point is as follows:

$$\%Error = \left(\frac{T_{theoretical} - T_{measured}}{T_{theoretical}}\right) * 100 \quad (8)$$

Where:

$T_{theoretical}$ = Temperature obtained from algorithm (°C)

$T_{measured}$ = Temperature measured with IR laser thermometer (°C)

The theoretical value, $T_{theoretical}$, was obtained by averaging a 3x3 matrix of temperature values at each test point (see Figure 13). The results of this process may be seen below.

The following five temperature conversion equations were tested:

Table 2: Calibration equations tested

Calibration Method 1:	$-5 \cdot 10^{-6}x^2 + 0.1202x - 626.92$
Calibration Method 2:	$0.0338x - 254.31$
Calibration Method 3:	$\left(\left((0.05872x) - 479.23 + 75\right) - 32\right) * \frac{5}{9}$
Calibration Method 4:	$0.0217x + 23.8 - 177$
Calibration Method 5:	$0.0465x - 349.44$

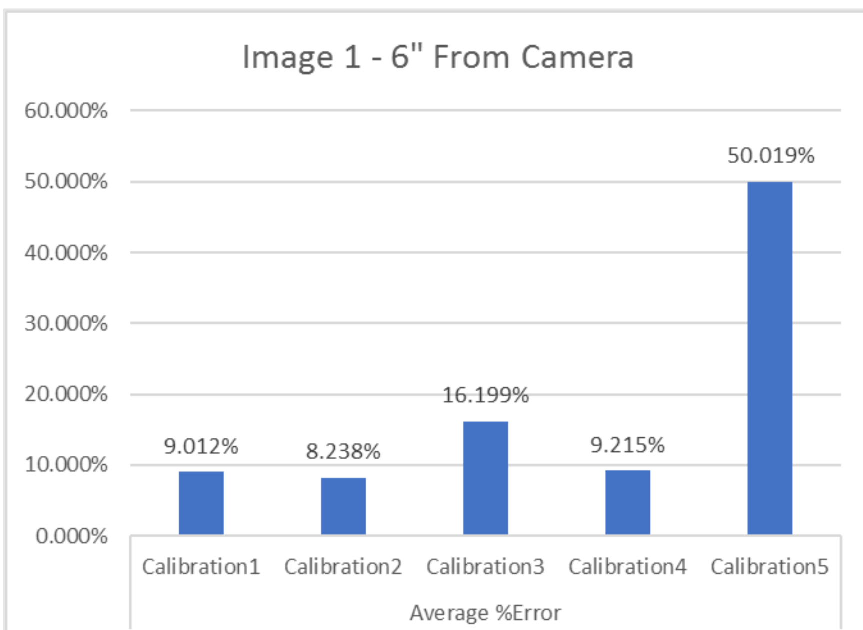

Figure 14: %Error of each calibration equation measured on test image at 6”

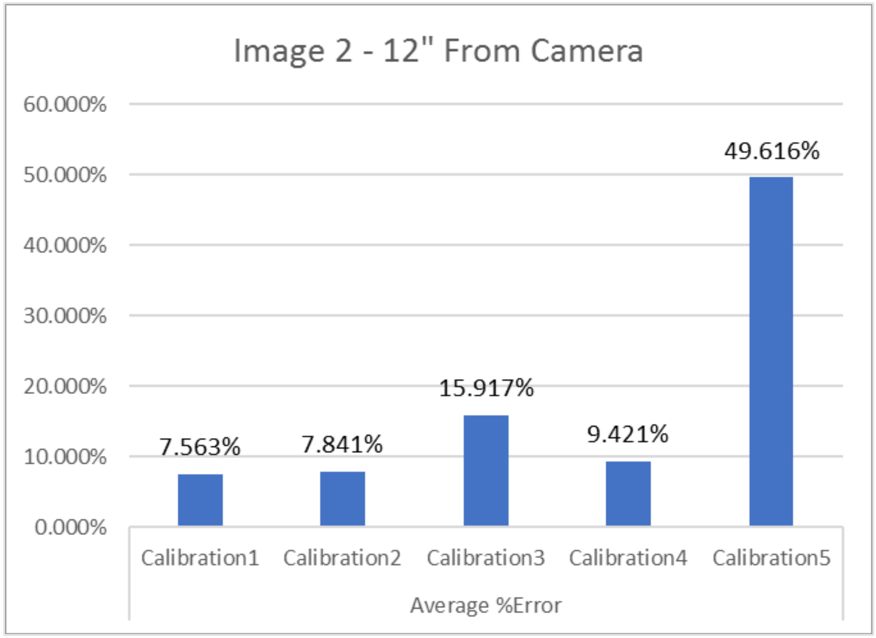

Figure 15: %Error of each calibration equation measured on test image at 12”

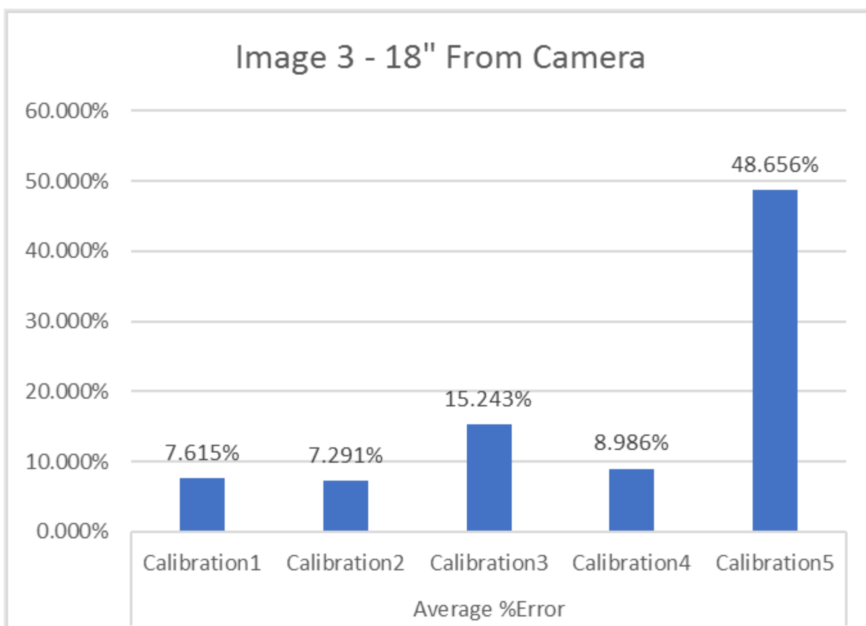

Figure 16: %Error of each calibration equation measured on test image at 18”

Each calibration method was evaluated and method 2 was chosen. Calibration method 2 had the lowest average % Error. The average % Error for each equation may be seen below.

Table 3: Average %Error of all calibration equations combined from each %Error obtained from each image (6”, 12”, and 18”)

Calibration 1	Calibration 2	Calibration 3	Calibration 4	Calibration 5
%8.0633	%7.7903	%15.7862	9.2076%	49.4302%

CHAPTER 4: SIMSCAPE SIMULATION MODEL

MATLAB R2016a was used to complete the necessary heat transfer simulations on various samples of bar stock. Images of the MATLAB Simscape model may be seen in Appendix D. Specifically, the following thermal elements were used from the 'Simscape' library to complete the simulation: Conductive Heat Transfer, Convective Heat Transfer, Thermal Mass, and Thermal Reference. Other elements included in the simulation include: Ideal temperature sources, Simulink Physical-Signal converters, and summing junctions.

4.1 THERMAL ELEMENTS

Conductive and convective heat transfer elements were the most common and important elements used for this simulation. "The Conductive Heat Transfer block represents a heat transfer by conduction between two layers of the same material. The transfer is governed by the Fourier law and is described with the following equation:"

$$Q = k \cdot \frac{A}{D}(T_A - T_B) \tag{9}$$

Where:

Q = Heat flow
K = Material thermal conductivity
A = Area normal to the heat flow direction
D = Distance between layers
T_A, T_B = Temperature of the layers

“The convective heat transfer block represents a heat transfer by convection between two bodies by means of fluid motion. The transfer is governed by the Newton law of cooling and is described with the following equation:”

$$Q = k \cdot A \cdot (T_A - T_B) \tag{10}$$

Where:

Q = Heat flow
K = Material transfer coefficient
A = Surface area
T_A, T_B = Temperature of bodies

In addition to these elements, a thermal reference element was used to provide MATLAB with a mass and specific heat for the most accurate simulation results. “The block represents a thermal mass, which is the ability of a material or combination of materials to store internal energy. The property is characterized by mass of the material and its specific heat.” The thermal mass may be described below in Equation 11.

$$Q = c \cdot m \frac{dT}{dt} \tag{11}$$

With these elements, the aluminum support structure and bar stock sample were simulated with a heating source wrapped around the center of the bar stock sample. A visual reference of the test sample and its dimensions can be seen below.

Figure 17: Aluminum test sample visual reference

Table 4: Aluminum test sample dimensions

Test Sample Dimensions		
	in.	**cm**
Length (l)	12	30.48
Width (w)	0.125	0.3175
Height (h)	0.75	1.905

For accurate simulations, the aluminum support structure was included because the bar stock sample contacts the aluminum structure at two points allowing heat conduction. Below represents the bar stock sample with all points noted of direct contact.

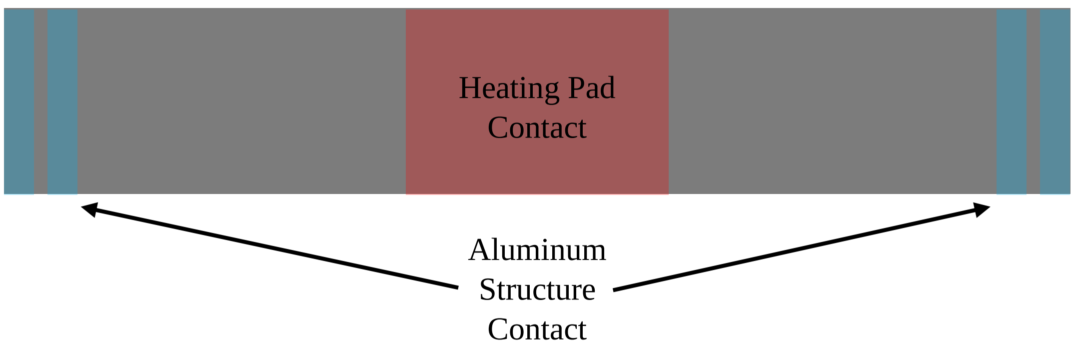

Figure 18: Aluminum test sample with contact areas highlighted: red – heating pad, blue – aluminum support structure

These points of contact are important to consider in the simulation because these represent conductive heat transfer/loss points. Heat will be transferred from the center of the object towards the points of contact with the aluminum structure. The simulation in MATLAB was set up with the following subsystems: Aluminum Support Structure, Bar stock, and Temperatures.

4.2 SIMULATION SUB-MODELS

4.2.1 ALUMINUM SUPPORT STRUCTURE

The aluminum support structure subsystem consists of 2 different elements. The first being a convective heat transfer element. Even though the aluminum structure is making direct contact with the bar stock meaning that, technically, the heat transfer between the two different metals is conductive, it is simulated as convective. This is due to the differences in properties of the convective heat transfer element and the conductive heat transfer element. The conductive heat transfer element requires a thickness and, for this application, there is not a thickness. To compensate for the difference between conductive and convective heat transfer, it was assumed that a heat transfer coefficient of 200,000 W/(m^2*K). Below in Table 5, the full list of parameters for the convective heat transfer element can be seen.

Table 5: Convective heat transfer parameters for surface contact with aluminum support structure

Property		**Units**
Area	0.00028079	m^2
Heat Transfer Coefficient	200,000	W/(m^2*K)

The area was derived from the following:

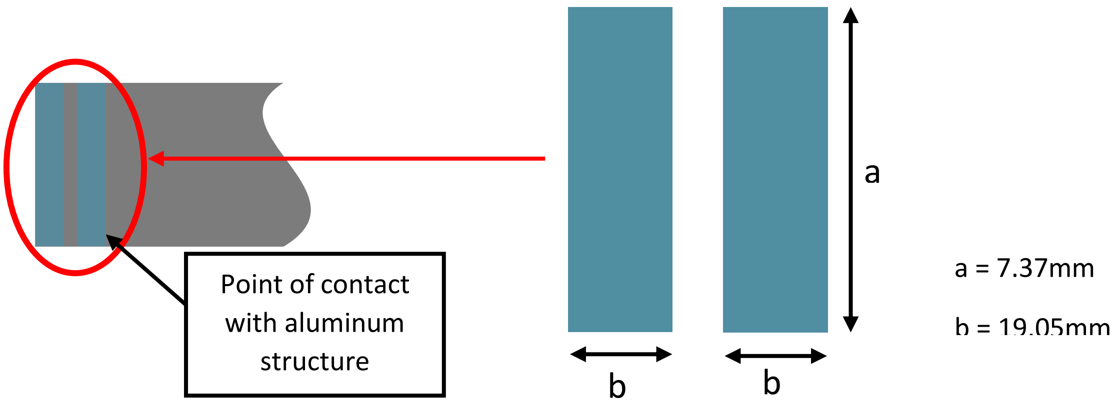

Figure 19: Dimensions of area in contact with surface of aluminum structure

$$\text{Contact Surface Area} = 2 * (l * w)$$
$$= 2 * (a * b)$$
$$= 2 * (7.37mm * 19.05mm)$$
$$= 280.797mm^2$$

After calculating the surface area that the bar stock sample contacts the aluminum structure, the thermal mass was calculated simply weighing the aluminum structure. This weight equaled 0.36lbs or 0.81646kg. The parameters, as entered in their respective elements can be seen below.

Table 6: Simulation parameters for convective heat transfer between aluminum test subject and the aluminum support structure

Convective Heat Transfer Element		
		Units
Area	$280.797*10^{-3}$	m^2
Heat Transfer Coefficient	$200*10^3$	$W/(m^2*K)$
Thermal Mass		
Mass	0.816466	Kg
Specific Heat	896	J/kg/K

The heat source temperature is used as the input temperature source to the bar stock sample while the room temperature is used for simulating convective heat losses from the aluminum structure and bar stock sample. The elements contained in this model are: Constants, Summing junctions, Simulink to physical signal converter, Ideal temperature source, and Physical model connection ports. To simulate a physical signal in MATLAB, a Simulink to physical signal converter must be used to convert constants into actual signals. After each signal is converted into a temperature, the signal then passes through a port on the subsystem that is connected to the bar stock sample.

4.2.2 BAR STOCK TEST SAMPLE

The bar stock example section includes 11 sections total. There are three different types of sections included in this complete model of the bar stock. These sections include two end sections where the bar stock sample meets the aluminum support structure (1 and 11), the middle section where the heating pad is applied directly to the bar stock (6), and the sections exposed to ambient air (2,3,4,5,7,8,9, and 10).

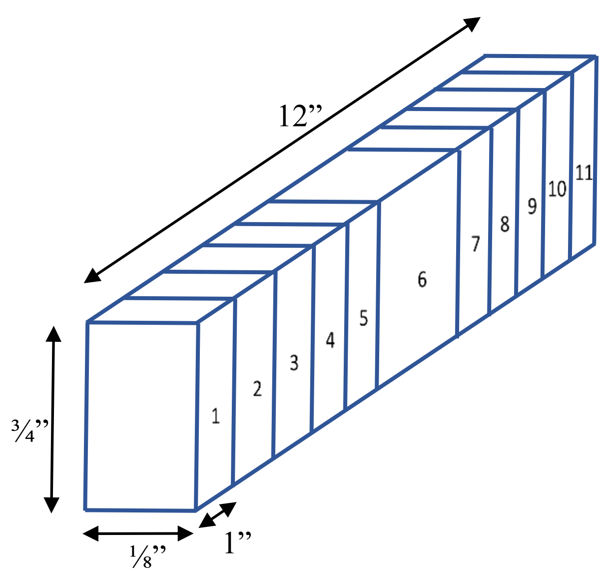

Figure 20: Aluminum test subject sectional breakdown used when simulating in Simscape

Sections 1 and 11 were modeled with a thickness of 1”, or 0.0127m total because that is the width of the contact area the bar stock sample makes with the aluminum structure. This was chosen because the convective heat flow elements used to simulate the heat flow from the bar stock sample to the aluminum structure was incorporated in these sections. Thermal mass elements were included in each of these sections to simulate the aluminum structure. Section 6 (See Figure 20) was the section designated for the heater measuring 2” wide in accordance with the heater dimensions and included a few extra elements including a temperature source measuring ideal temperature that the heater will reach at steady state. Sections: 2, 3, 4, 5, 7, 8, 9, and 10 are identical sections that were used as reference points to measure temperature and included conductive and convective heat transfer elements. With this model created and all parameters entered, simulation results could be obtained and are described in Chapter 7.

CHAPTER 5: CODE DEVELOPMENT

5.1 IMAGE ACQUISITION

Stated earlier, sample code was used as a foundation for the code to capture a thermal image from the camera. The code was created by Pure Engineering LLC and provides users with a starting point to communicate with the FLIR Lepton camera module using the communication protocols SPI and I2C. One of the most important features of the reference code includes a built-in histogram-based algorithm for automatic gain control (AGC). The AGC algorithm is used to map gray shades to the "portions of the input range occupied by the most pixels." Every time an image is captured, the algorithm adjusts the grayscale so that different shades may be applied based on the highest percentage of data points that are similar. An example image using this algorithm may be seen below.

Figure 21: Histogram techniques: Linear AGC (LEFT), Classic Histogram Equalization (CENTER), Lepton's Variant of Histogram Equalization (RIGHT)

Another function that the reference code serves is acquiring the image payload. The payload can be broken down into three main parts: a packet, a frame, and a stream, all of which are acquired from the camera to the Raspberry Pi using SPI communication protocol. A packet consists of data for a single line of an image. A frame is a continuous sequence of 60 packets total comprising a full image. A stream is a continuous sequence of an arbitrary number of frames captured in sequence. A visual reference of these terms may be seen below.

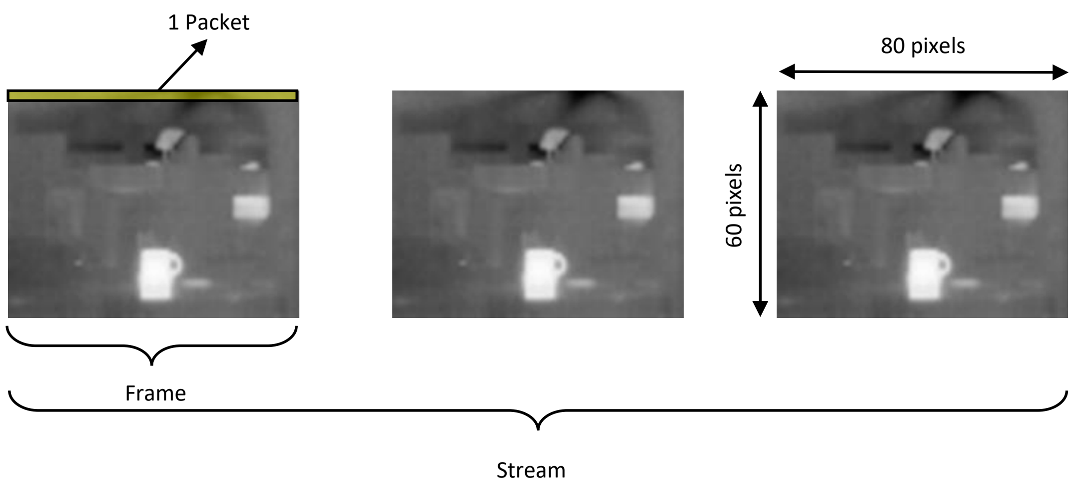

Figure 22: Visual representation of frame packet, individual frame, and frame stream acquired from FLIR Lepton camera

Imagine each frame seen above was captured in sequence with the FLIR Lepton camera. The highlighted row in the first frame is a packet of data. The complete image is considered a frame. While the complete sequence is considered a stream. The reference code handles each data point (pixel) captured and creates a packet. Each packet is then indexed forming the complete image packet using the packet ID. The packet ID dictates the order of the packets in a frame. The packet structure can be seen below.

Table 7: Packet ID description acquired by FLIR Lepton camera

ID	CRC	Payload
4 bytes		160 bytes

The Cyclic Redundancy Check (CRC) field is generated using the following polynomial:

$$x^{16} + x^{12} + x^{5} + x^{0} \tag{12}$$

This is used so there aren't any redundant frames in an image. Overall, the sequence of operations for capturing an image may be described with the flowchart below:

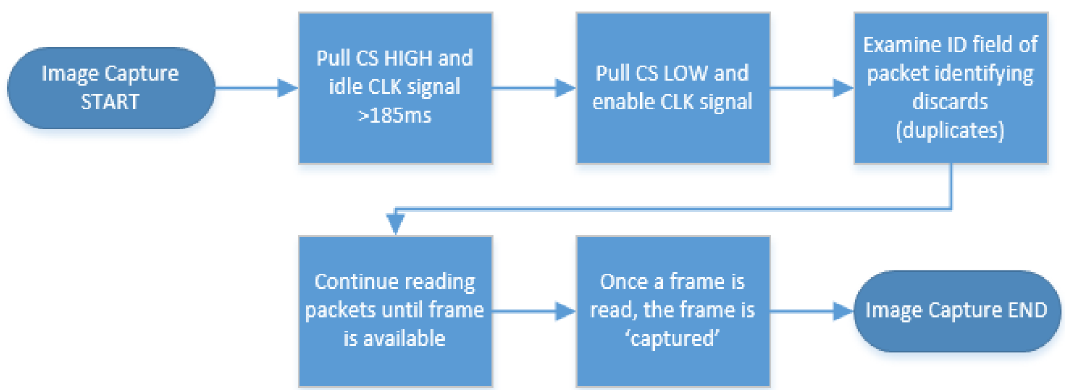

Figure 23: Flow diagram depicting the image acquisition process of the FLIR Lepton camera

Each of these steps play a crucial role in capturing an image. Step 1 is performed to establish synchronization with the FLIR Lepton camera. The Chip Select (CS) is pulled high ≥185ms to ensure a full timeout of the SPI interface to avoid any synchronization issues. Step 2 is performed to establish communication with the camera by asserting the CS so that packets from the camera may be transmitted. To read each packet in the correct order, step 3 identifies the ID field of each packet and discards any duplicate packets so that a full frame may captured. Once a frame is available, it is transmitted over SPI to the host controller, in this case, a Raspberry Pi. By default, the frame that is captured and transmitted has the Lepton histogram algorithm applied. The goal of modifying the code given was to perform the underlying functions necessary to convert a frame of raw pixel data into a frame of temperature values. The steps used to complete this process are as follows:

1. Capture an image
2. Obtain raw pixel data before Lepton histogram correction is applied
3. Apply an algorithm converting raw pixel data into temperature values

To read the pixel data of a frame, a .txt file was created. The code was used to capture a single frame of pixel data. A .txt file was created to capture the array of pixel data. To create the .txt file, the code seen in Figure 24 was used.

```
    do {
        sprintf(image_name, "IMG_%.4d.pgm", image_index);
        image_index += 1;
        if (image_index > 9999)
        {
            image_index = 0;
            break;
        }

    } while (access(image_name, F_OK) == 0);
```

Figure 24: C code used to create the .txt file containing raw data pixel data from FLIR Lepton camera

With this code, a .txt file was created every time this code was executed. Every time the code was executed the image number was indexed so the previous .txt file containing pixel data was not overwritten so this code could be executed up to 9999 times without an overwrite. The number of files, 9999, was a maximum number that would never be reached for this experiment. Next, an array containing each pixel was created. Each pixel was captured indexed to create the 60x80 array of the frame.

```
    for(i=0;i<60;i++)
    {
        for(j=0;j<80;j++)
        {
            fprintf(f,"%d ", lepton_image[i][j] - minval);
        }
        fprintf(f,"\n");
    }
    fprintf(f,"\n\n");
```

Figure 25: C code used to form frame comprised of raw pixel data captured from FLIR Lepton camera

In lines 100-102, each pixel (array element) is indexed so that the Lepton histogram algorithm may be implemented. The minimum value and maximum value of the raw pixel data is calculated to set the range of values for each pixel. An example of this may be seen below.

8124	8121	8119	8124	8124	8118
8122	8119	8124	8127	8121	8118
8123	8120	8122	8124	8118	8120
8126	8120	8118	8121	8118	8113
8120	8117	8117	8119	8118	8113
8123	8117	8117	8119	8113	8110
8120	8114	8116	8115	8116	8115

48	45	43	48	48	42
46	43	48	51	45	42
47	44	46	48	42	44
50	44	42	45	42	37
44	41	41	43	42	37
47	41	42	43	37	34
44	38	40	39	40	39

Figure 26: Raw pixel data to temperature (°C) conversion example

Above are two 7x6 arrays of pixel data. On the left, raw pixel data is shown, while on the right, converted pixel data is shown. The values on the right were calculated based on the minimum pixel value and are used in Leptons histogram algorithm. The values that were used in converting each pixel into a temperature value were raw pixel values so that's why these values were the main point of concern instead of the processed values. To capture raw pixel values, modifications needed to be performed to output a .txt file containing these values. To do this, the following code was added.

```
100.     for(i=0;i<60;i++)
101.     {
102.             for(j=0;j<80;j++)
103.             {
104.                     fprintf(f,"%d ", lepton_image[i][j]);
105.             }
106.             fprintf(f,"\n");
107.     }
```

Figure 27: C code used to auto-index each raw pixel data value into a matrix

Here, each element of the frame captured is printed to an array ignoring the values related to the histogram. Two for loops were used to index through each element of the frame and print the pixel data. By doing this, each raw value was written into a 60x80 array, the same size as a frame.

With the correct calibration method selected, the equation was then applied so that once an image is captured, the temperature values for each pixel may be output into a .txt file. The following code was used to create the .txt file with temperature values.

```
for(i=0;i<60;i++)
{
      for(j=0;j<80;j++)
      {
            lepton_temp_image[i][j] = lepton_image[i][j];
            fprintf(a,"%0.2f ", (0.0338*lepton_temp_image[i][j]) - 254.31);
            //fprintf(a,"%d ", lepton_image[i][j]);
      }
fprintf(a,"\n");
}
```

Figure 28: C code used to auto-index each temperature value into a matrix

In these nested for loops, each pixel is indexed and input into a 60x80 array containing the temperature values. The variable 'Lepton_temp_image[i][j]' represents the pixel element obtained from the FLIR Lepton. The equation was then applied to each element of the frame creating a 60x80 array of temperature values representing each pixel in the frame.

5.2 IMAGE PROCESSING

Once the .txt containing the 60x80 matrix of temperature values was created, the next step was to apply image processing techniques using MATLAB software. A script was created in MATLAB to do this. First, the .txt file was loaded into MATLAB. The image was enlarged using the ‘bilinear’ method. This method enlarges the image creating more pixels by averaging the nearest 2x2 matrix of pixels. This averaging method causes the least amount of temperature distortion of the image when resizing. Using this method, the 60x80 image becomes a 480x640 pixel image. In addition, the image pixel info was made available so that by hovering over the image with a mouse cursor reveals the temperatures wherever their cursor is located. An example of this can be seen below. The pixel of interest in this image is represented by a red dot located to the left of the heater.

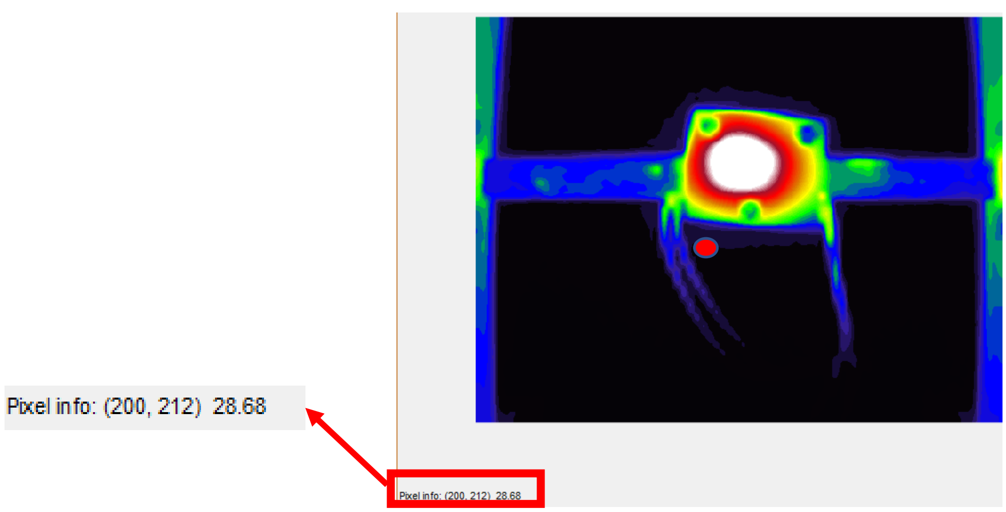

Figure 29: Temperature data available on processed image

A colormap was applied to the image to give students a range of colors related to temperature values present in the image. For this experiment, the practical range of temperatures was recorded from 20°C - 75°C. A custom colormap was created and applied to the image. Values in increments of five was added to the colormap to give students temperatures they could relate to those present in the image. An image captured with the colormap applied can be seen below.

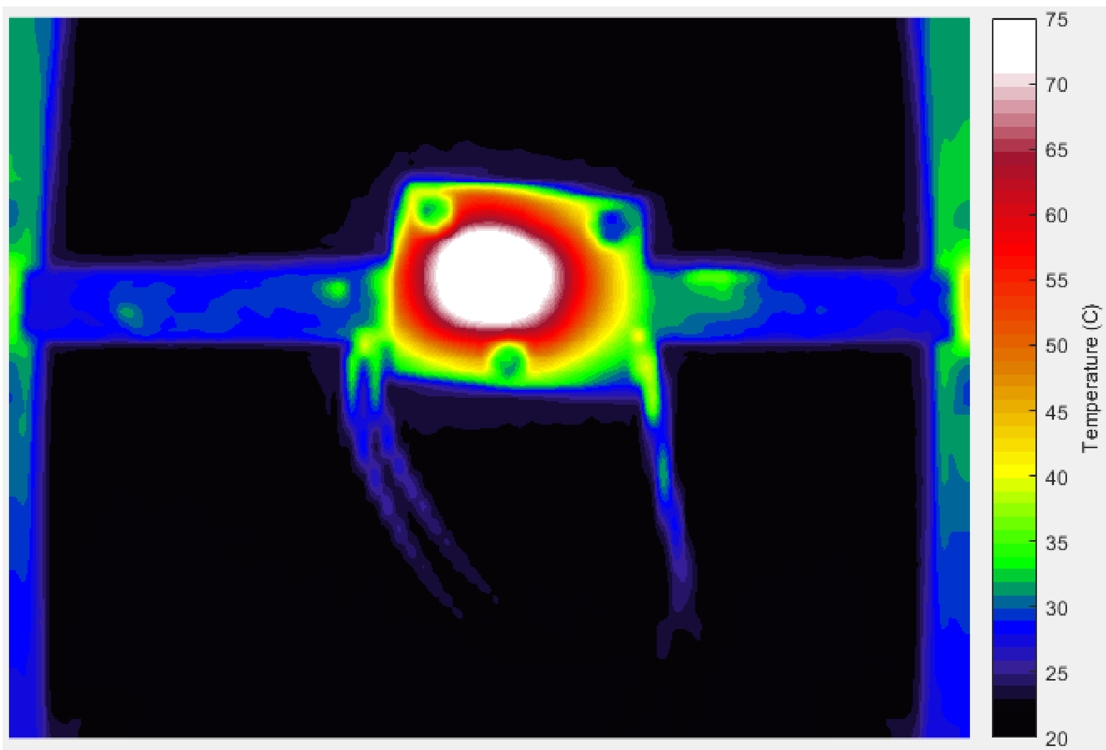

Figure 30: Processed thermal image acquired from FLIR Lepton camera including custom colormap

Next, A graph was created depicting temperature vs. pixel of the image. This graph was created by taking a 1x80 array of temperatures on the test sample and graphing them using MATLAB. A graphical representation of this may be seen below.

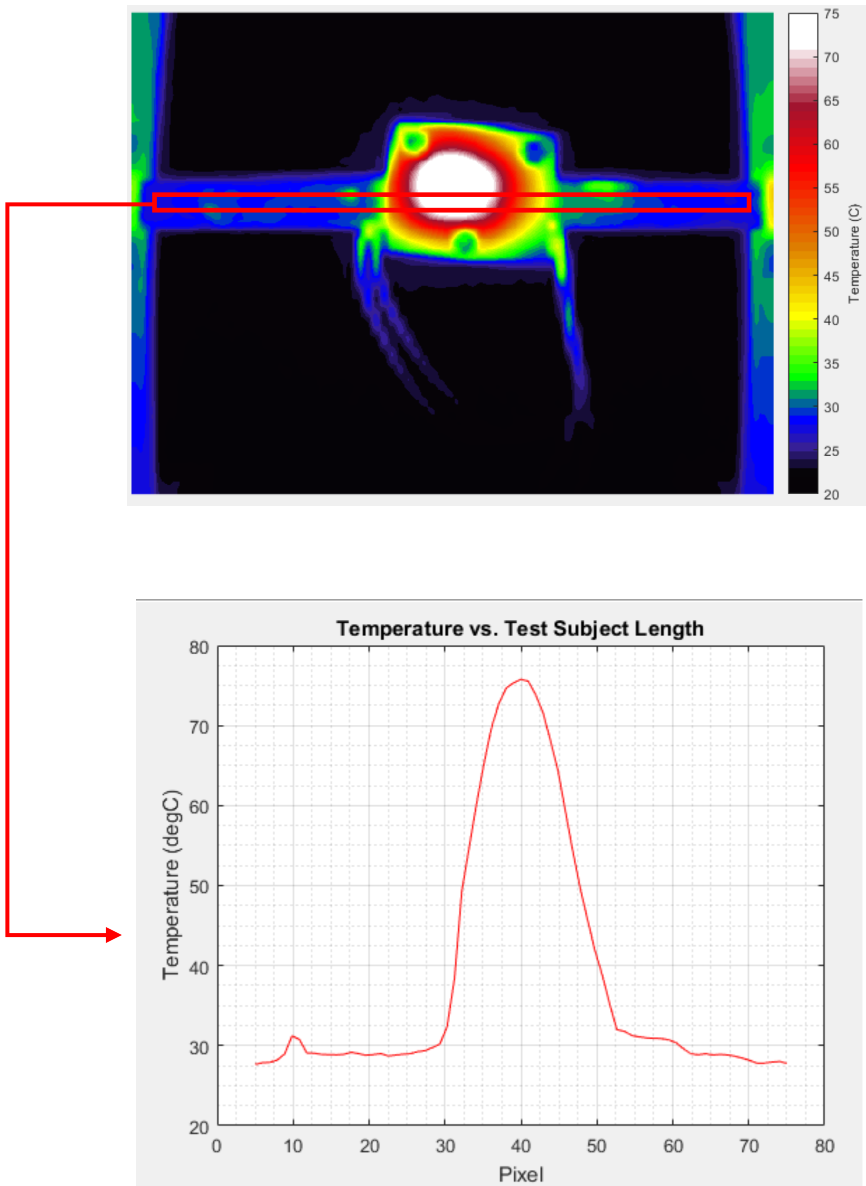

Figure 31: Acquisition process of temperature graph related to pixel value of camera

Using these tools, enough information was provided to make an educated decision on whether or not a test sample has a defect or not. The tools provided to students include:

- Thermal image
- Temperature data related to the pixel of the image
- Custom colormap of temperatures present in the image
- Graphical representation of the heat transfer through the test sample

CHAPTER 6: RESULTS

6.1 TNDT Thermal Model

Simulations were performed using MATLAB to determine which material would be used in the laboratory experiment. Quantitative data was collected for different defect dimensions. Each material was subject to the same defect while temperatures were measured over time to determine the material that would best suit the experiment. Some important considerations that were necessary to account for were: time to reach steady-state temperature, the magnitude of temperature differential at specific points, and material properties used during simulations. Initial simulations implied Aluminum would be the best sample material because it had the greatest thermal performance considering the criteria listed above.

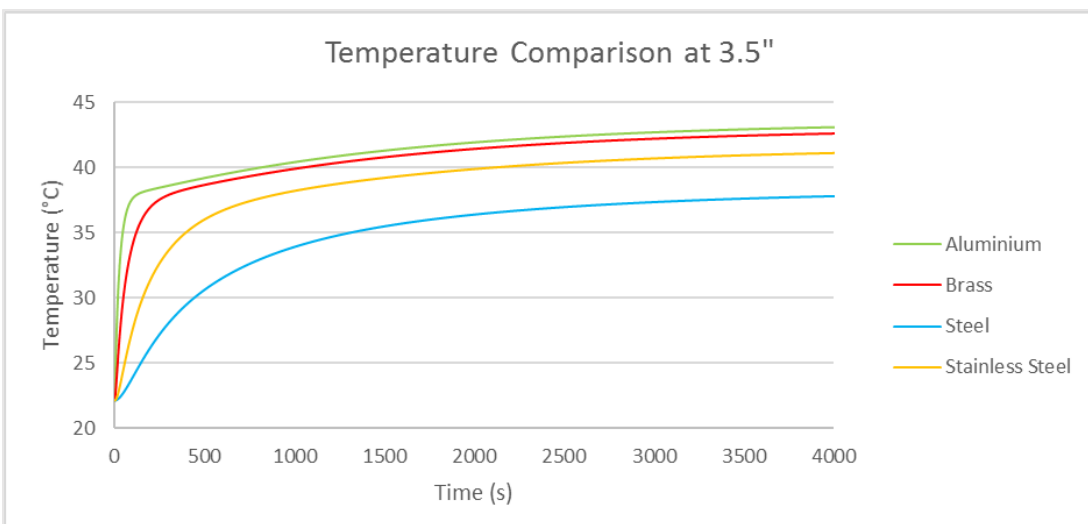

Figure 32: Simulated temperature comparison of a test point located at 3.5” on an ideal sample of aluminum, brass, steel, and stainless steel

Four different defect measurements were measured and simulated. Multiple defects were simulated to choose the ideal defect size that would result in a subtle temperature differential around the location of the defect. This would force students to think critically and apply analytical skills to make the correct decision when choosing which sample is defective. Even though aluminum out-performed the other materials with initial simulations, the defects were simulated with all materials to verify aluminum was the correct choice to pursue for experimental design. The following defects were chosen to be simulated:

Table 8: Defect dimensions

	Width		**Depth**		**Height**	
	cm	in.	cm	in.	cm	in.
Defect 1	0.3175	1/8”	0.15875	1/16”	1.905	3/4”
Defect 2	0.635	1/4”	0.15875	1/16”	1.905	3/4”
Defect 3	1.27	1/2”	0.15875	1/16”	1.905	3/4”
Defect 4	1.27	1/4”	0.238125	3/32”	1.905	3/4”

In this section, simulation results depict each material’s thermal characteristics in two different ways. First, a graph measuring temperature at specific locations on the test sample. Second, a graph measuring temperature differential using references from the half of the sample without the defect minus the half of the sample with the defect. A visual reference with an example subtracting temperature at 0.5” from 11.5” may be seen below.

$$Temp. Differential = Temp. @\ 0.5" - Temp. @\ 11.5"$$

Figure 33: Temperature differential of temperatures equidistant from center of test sample

6.1.1 STEEL SIMULATION RESULTS

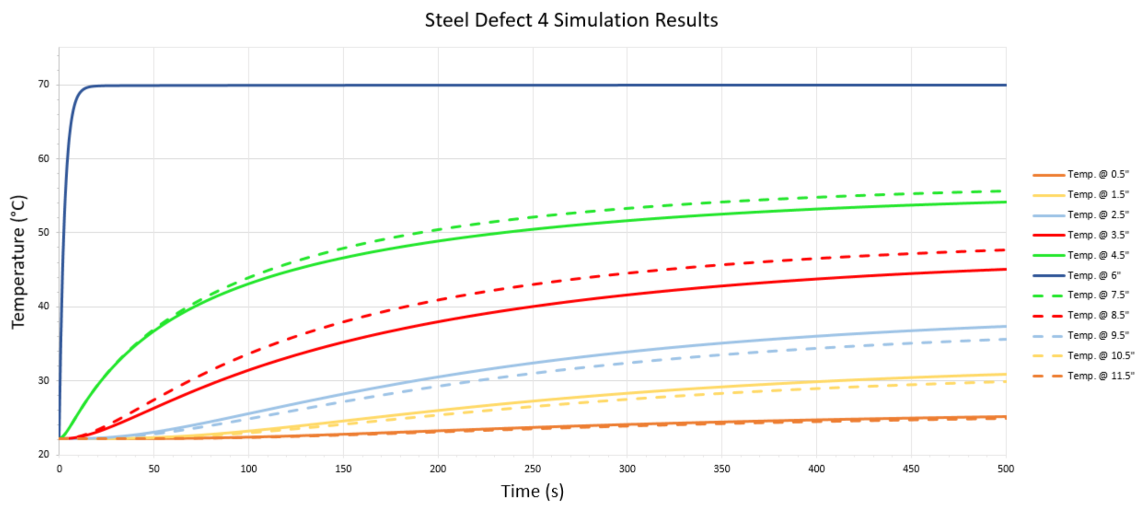

Figure 34: Thermal response of steel defective sample simulated with a heater temperature of 70°C

When simulating steel, the following material properties were used:

- Thermal conductivity = $43\frac{W}{m*K}$
- Specific heat = $510.7896\,\frac{J}{kg*K}$.

Heat flow has a linear relationship with the magnitude of thermal conductivity meaning steel does not conduct well because of its low thermal conductivity. Even though steel does not appear to be a good candidate, this graph indicates one could distinguish the general location of the defect for this bar stock sample. Knowing the dotted lines indicate temperatures relative to the half of the sample without the defect, one can conclude that the defect is between 8.5” and 9.5” from this graph

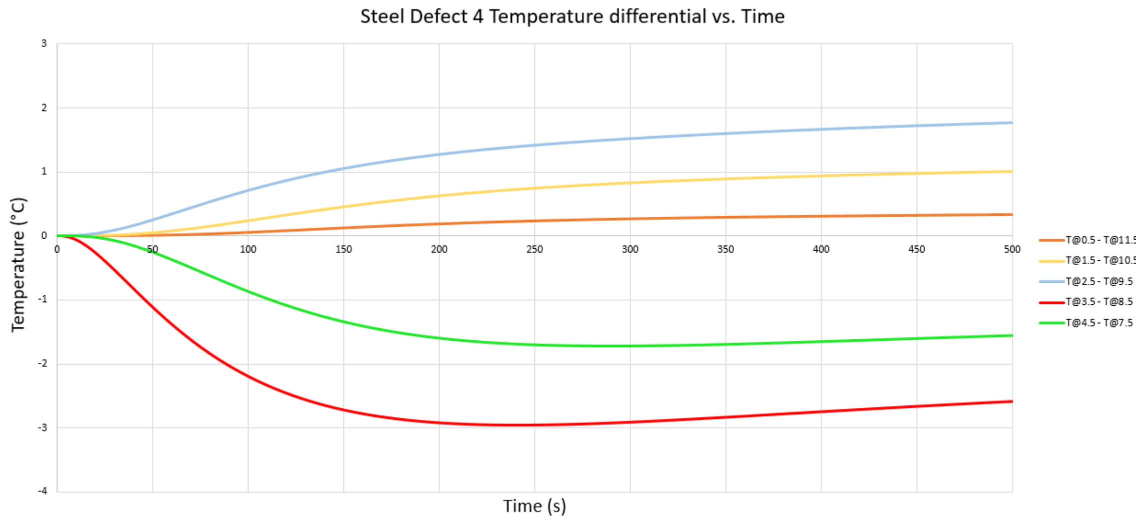

Figure 35: Temperature differential of steel defective sample simulated with a heater temperature of 70°C

For steel, the greatest magnitude of temperature differential occurred at a time of 216s.. The maximum temperature differential was found by sampling all temperature measurements at 1s intervals measuring the greatest magnitude of temperature difference. This turns out to have a magnitude of 3°C. For this experiment, the sooner this temperature differential reaches its maximum the better. This material was not chosen due to its performance under time constraints and the time it takes to reach the maximum temperature differential.

6.1.2 STAINLESS STEEL SIMULATION RESULTS

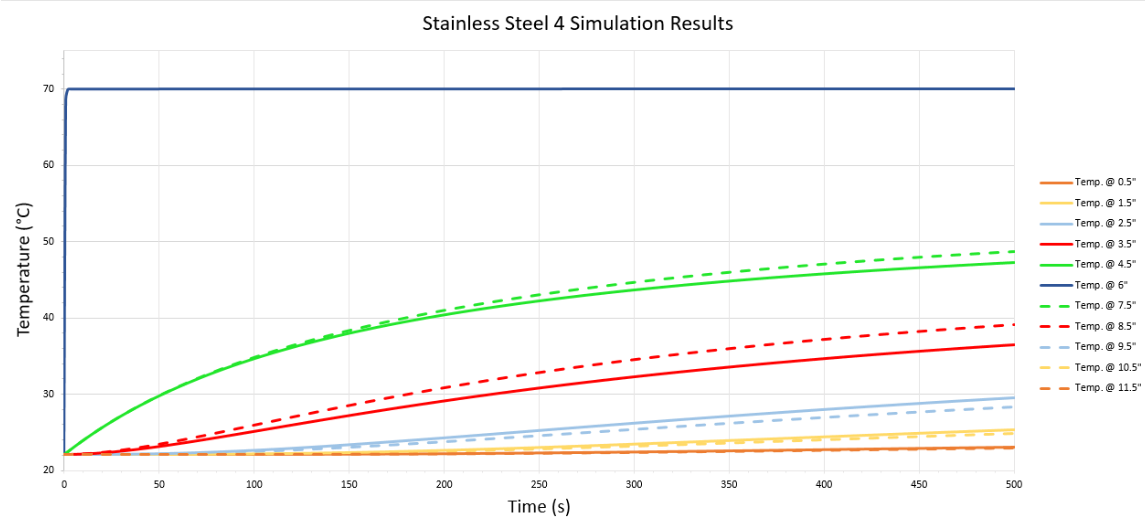

Figure 36: Thermal response of stainless steel defective sample simulated with a heater temperature of 70°C

Like steel, stainless steel was tested as a possible candidate as a material to be used for the bar stock sample. In the graph above, temperatures were recorded at 1” intervals starting at 0.5” equidistant from the center of the sample. The material properties used in the simulation for stainless steel are:

- Thermal conductivity = $16\frac{W}{m*K}$
- Specific heat = $502.416\frac{J}{kg*K}$.

The temperatures sampled at 4.5” and 7.5” rise rather quickly to temperatures noticeably different than ambient temperature, however, temperatures sampled at distances of 3.5” equidistant from the center only increase an average of 0.0164°C/s maximum rising a total of 8.2°C over 500s.

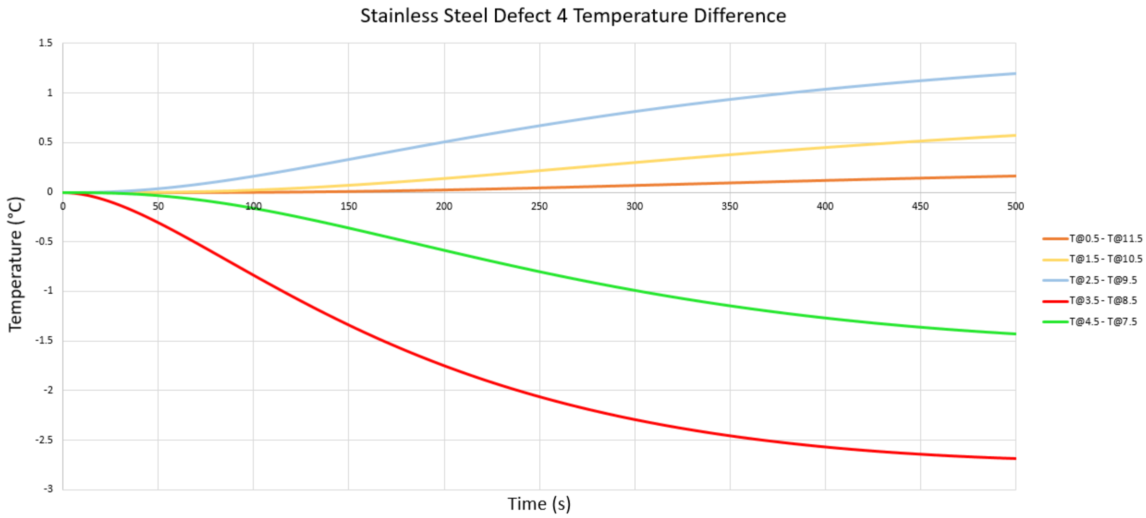

Figure 37: Temperature differential of stainless steel defective sample simulated with a heater temperature of 70°C

Stainless steel had the lowest thermal conductivity of all the samples simulated. According to the simulations, stainless steel had the worst result relative to time taken to reach maximum temperature differential. The total time to reach maximum temperature differential was 500s with a magnitude of 2.7°C. For each location temperatures were sampled, the maximum temperature differential for equidistant points was recorded at 500s. This indicates that the maximum temperature differential of each temperature measurement recorded could not be achieved during this simulation time. It was because of the poor temperature differential results along with poor heat transfer throughout the bar stock model that stainless steel was not used as the sample implemented in the laboratory experiment.

6.1.3 BRASS SIMULATION RESULTS

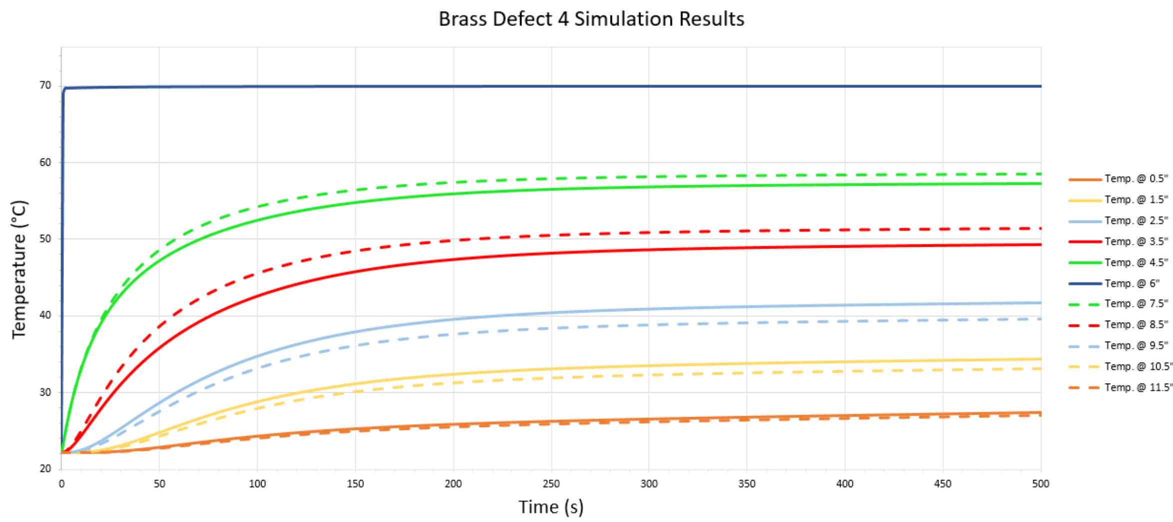

Figure 38: Thermal response of brass defective sample simulated with a heater temperature of 70°C

When simulating brass, the following material properties were used:

- Thermal conductivity = $109\frac{W}{m*K}$
- Specific heat = $401.933\frac{J}{kg*K}$.

Brass had favorable simulation results, however, the initial rise time was slower than aluminum due to its low thermal conductivity. The max temperature achieved was measured at 7.5” on the sample measuring 58.51°C. Although the temperature is rising at 500s, the maximum temperature never passes that of aluminum. In this graph, it can be seen that the defect is between 8.5” and 9.5” clearly. This is determined when the temperature measured on the side of the defect drops below the temperature measured on the side without the defect equidistant from the center of the sample.

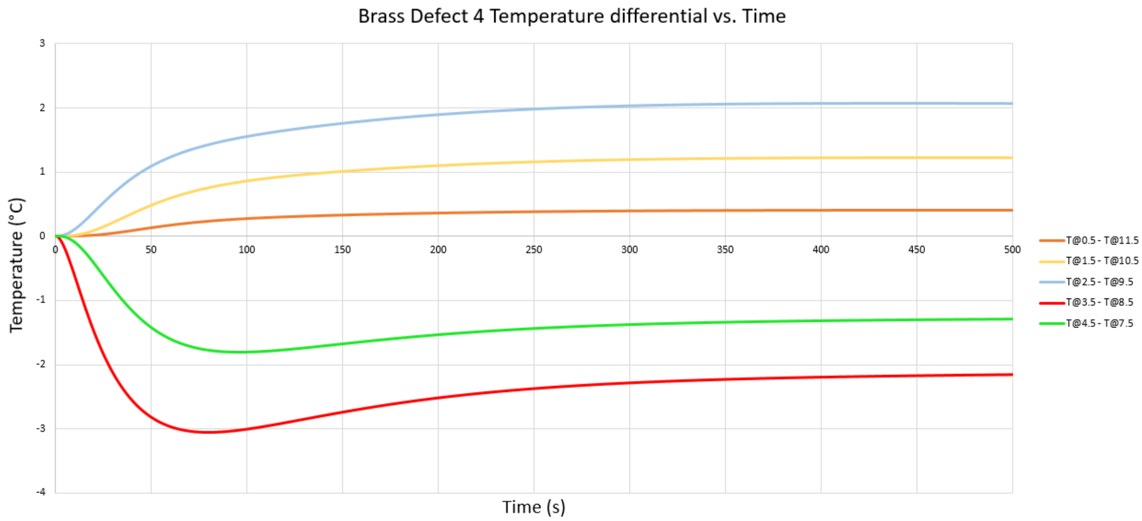

Figure 39: Temperature differential of brass defective sample simulated with a heater temperature of 70°C

Simulations depict the time to reach steady-state is around 250s. The time it takes to reach maximum temperature differential is 80s. The maximum magnitude of temperature differential is 3.06°C. Negative values are used to help depict the location of the defect. Again, when the temperature differential becomes positive, one may assume that the defect is at the location the temperature is less than that being subtracted from. For example, focusing on the temperature differential of T@2.5" – T@9.5", the temperature differential is positive. This is due to the fact that there is less heat at 9.5" than 2.5". The temperature differential measured between 3.5" and 8.5" is positive. Knowing these two measurements, one may assume that the defect is located between 8.5" and 9.5". Less heat is present at 9.5" because the area is less between these two locations causing noticeable heat loss.

6.1.4 ALUMINUM SIMULATION RESULTS

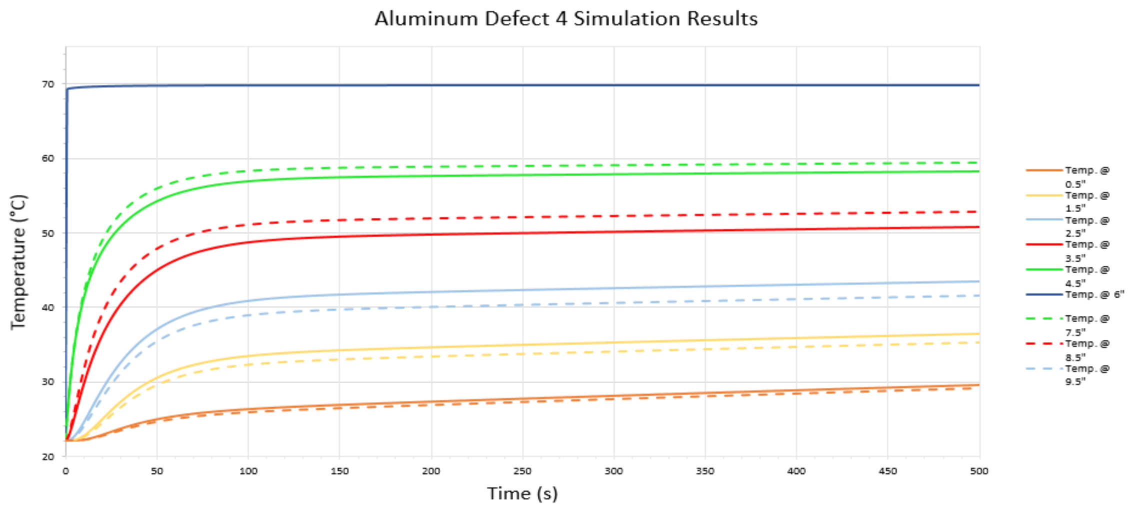

Figure 40: Thermal response of aluminum defective sample simulated with a heater temperature of 70°C

When simulating aluminum, the following material parameters were used:

- Thermal conductivity = $205\frac{W}{m*K}$
- Specific heat = $915\frac{J}{kg*K}$.

Compared to steel, stainless steel, and brass, aluminum has the greatest conducive thermal conductivity and specific heat properties. Seen in the graph above, all temperatures had a uniform rise pattern with temperatures increasing rapidly and leveling out around 100s into the simulation. Using Excel, linear regression was utilized to model temperature and time. The average steady-state temperature rise of each temperature measurement recorded was 0.0052 °C/s with a R2 value of 0.971. This is over three times the maximum temperature progression of stainless steel. Due to this simulation response depicting high heat conductivity properties, aluminum was confirmed as the material of bar stock to be tested.

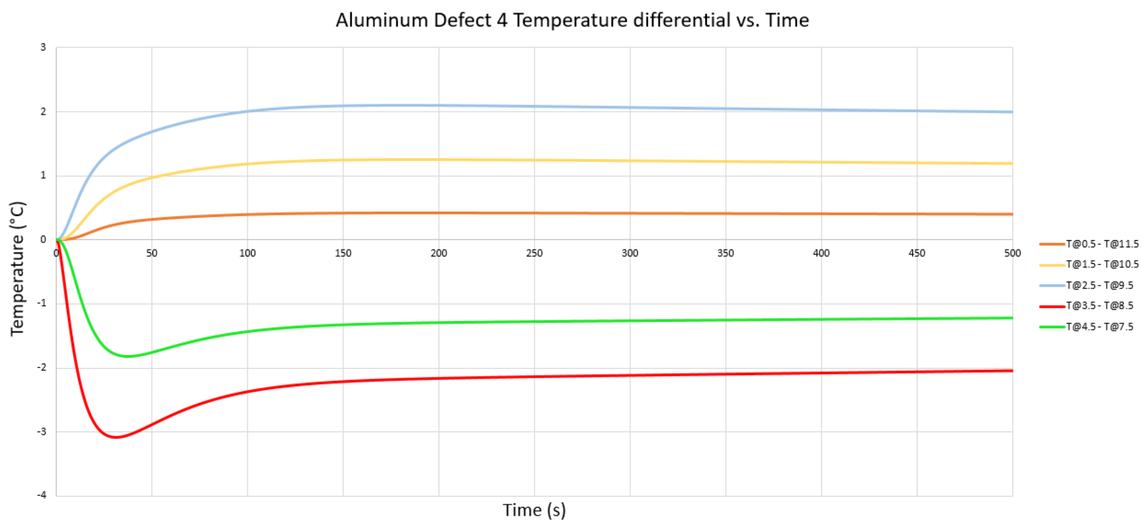

Figure 41: Temperature differential of aluminum defective sample simulated with a heater temperature of 70°C

Figure 41 depicts the temperature differential of temperatures equidistant relative to the center of the sample – 6”. Out of all the materials simulated, aluminum has the fastest time to reach maximum temperature differential measured at 31s with a magnitude 3.08°C. It is important to note that these temperatures are taken relative to the magnitude of temperature present at each measurement location on the sample and not to ambient temperature. This was done in order to compare temperature readings measured near the defect and temperature readings measured further away from the defect both being equidistant from the center of the sample to form a relationship between the two. This relationship is depicted in the graph above and clearly shows the general location of the defect. Aluminum, in particular, displays this relationship well compared to the other materials by providing a predictable temperature differential and temperature rise after 100s.

6.2 ALUMINUM TNDT MEASURED RESULTS

Two aluminum samples were tested using the FLIR Lepton camera to compare results from simulation models. This was achieved by applying two heating pads directly on the surface of the aluminum test subject and capturing thermal images at various time intervals. Each test sample may be seen below.

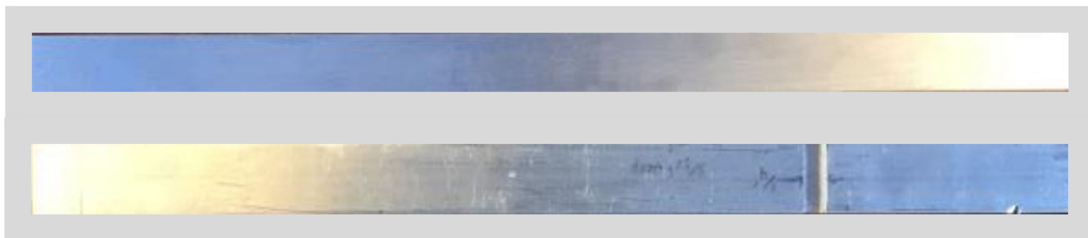

Figure 42: Aluminum bar stock test samples: Ideal (TOP), Defective (BOTTOM)

The heating pads were applied directly to the sample using two wooden fabricated pieces with three holes allowing hardware to tighten down each piece. This allows the entire surface of the heater to be applied directly to the sample resulting in minimal heat losses. A script was then used to simultaneously cycle power to the heater and capture thermal images at specified time intervals.

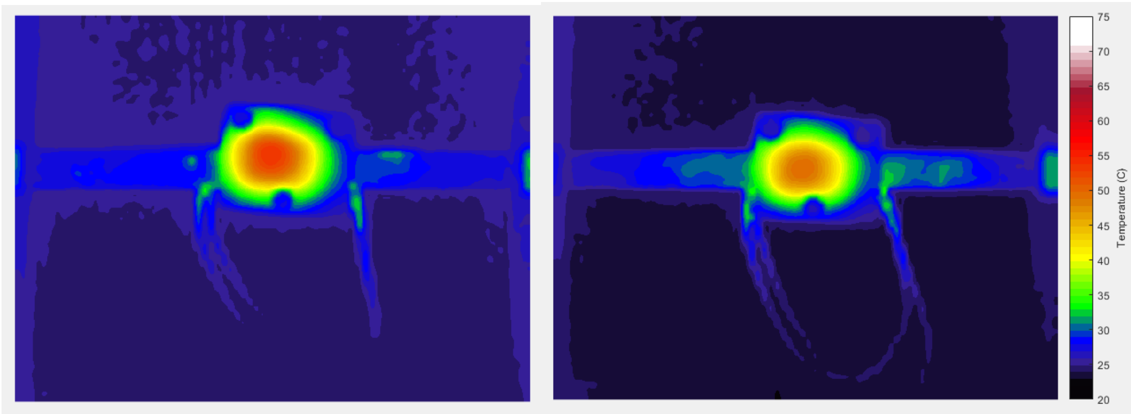

Figure 43: Thermal image comparison captured at time of 180s: Ideal sample (LEFT), Defective sample (RIGHT)

In the measured results, the initial heat load could not be overcome causing an increase in time to reach steady-state temperatures compared to simulations. The images above were captured at 180s. The heating pads were supplied with the rated 120V in the transient phase of heating. Once the desired steady-state temperature of ≈70°C was achieved, a PWM signal controlled power to the heaters to maintain this temperature. The samples were placed around 12" away. The image on the left depicts the ideal sample while the image on the right represents the defective sample. Already at this time, a difference can be seen between the thermal pattern of each sample. Heat appears to flow at a quicker rate on the right half of the defective sample. Although heat is flowing at a faster rate on the defective sample, the rate of change, $\frac{\Delta T}{\Delta t}$, it does not compare to the rate of change acquired from the simulations. This will affect the total time of the experiment.

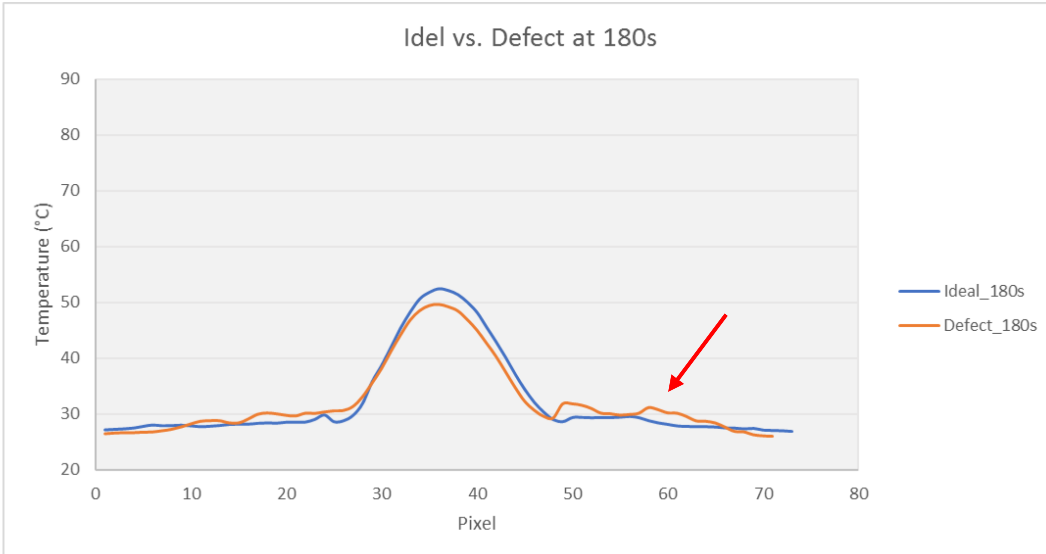

Figure 44: Temperature comparison taken at time of 180s across both samples: Ideal in Blue, Defective in Orange

Seen above is a graph representing temperature vs. pixels. The area area of interest, indicated by the arrow, shows the location of the defect. These results were obtained using a combination of MATLAB and Excel. A line graph was created based on a 1x60 array of temperatures taken from the length of the test sample. Noticeable changes in heat differential between the ideal and defective samples can be seen. The ideal sample has a uniform pattern whereas the defective sample shows signs of temperature inconsistency. This pattern does compare to simulations; however, the magnitude of the temperature differential is inconsistent. This inconsistency may be seen throughout thermal images and graphs depicted below.

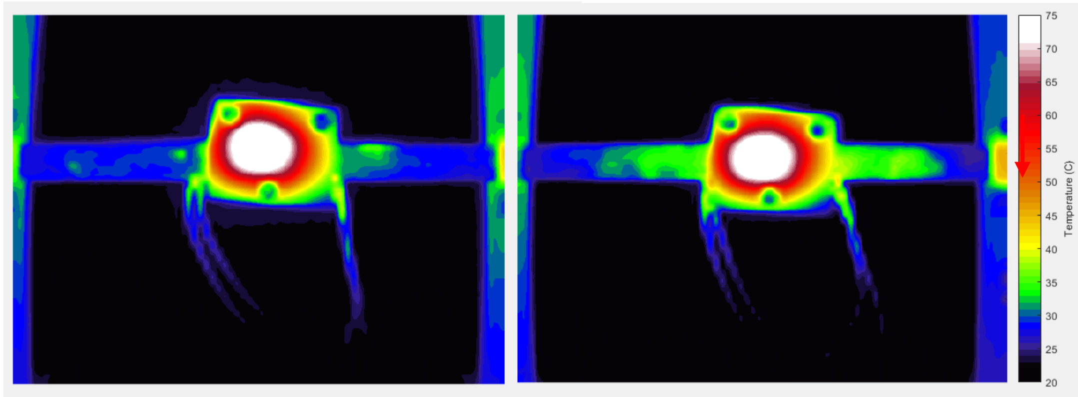

Figure 45 Thermal image comparison captured at time of 3180s: Ideal sample (LEFT), Defective sample (RIGHT)

Above, thermal images were captured at a time of 3180s. Again, the temperature rise time was increased in the experimental measurements due to the heating capacity allowed by the heaters and the heat load. The difference in temperature differential is more apparent in these images indicating a noticeable difference between the two test samples. Seen in the defective thermal image on the right-hand side, $\frac{\Delta T}{\Delta t}$ is increasing at a quicker rate than the left half of the sample. This is consistent with the simulations indicating some irregularity on the sample. The temperature rises into the 40°C range at the location of the defect highlighted in the image. The hotspots seen where the sample contacts the support frame structure are due to the bracket material used. The brackets were molded using rapid prototyping and the material has a higher emissivity causing these false hotspots. These are neglected using limits in the code when taking an array of temperature readings across the sample to create graphs of temperature vs. pixel.

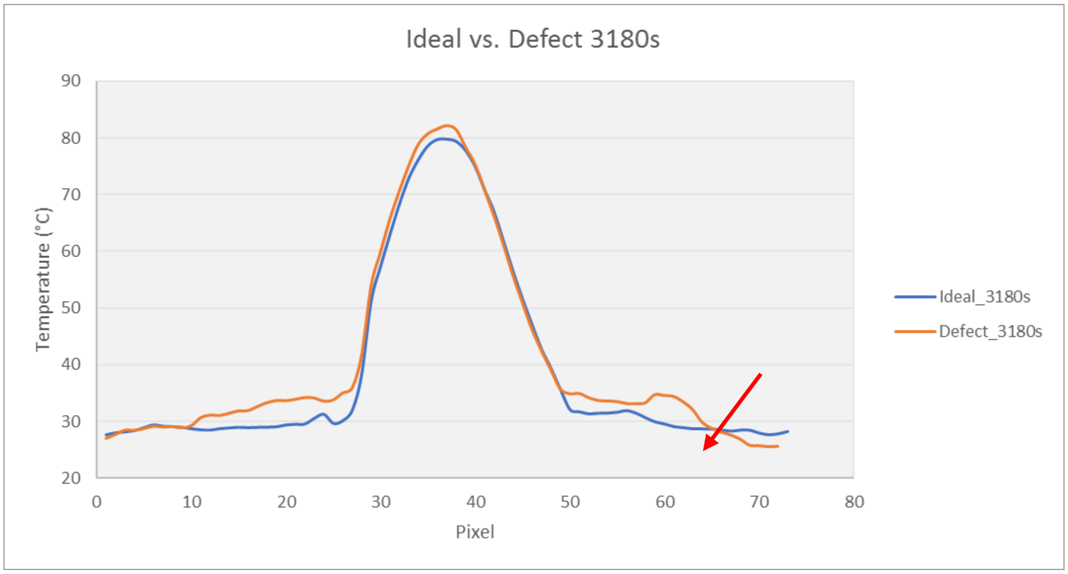

Figure 46: Temperature comparison taken at time of 3180s across both samples: Ideal in Blue, Defective in Orange

After heat was applied on the sample for 3180s (steady-state), both thermal images and the graph seen above were created. Compared to the previous graph, see Figure 44, this data further provides evidence of a defect present on the sample. The magnitude of temperature differential is at its greatest indicated by the red arrow. The location of the defect is also at this location. Recall that temperature is directly proportional to the area normal to heat flow. Because there is a defect, the area for heat to flow through the sample becomes less causing less overall heat flow. After the area of the defect, the area returns to normal resulting in normal heat flow to resume. The resulting temperatures mimic the expected result with a slight temperature decrease followed by an increase at the location of the defect. Even though this graph shows obvious signs of a defect, the temperature results are still not to the order of magnitude than those acquired by simulations.

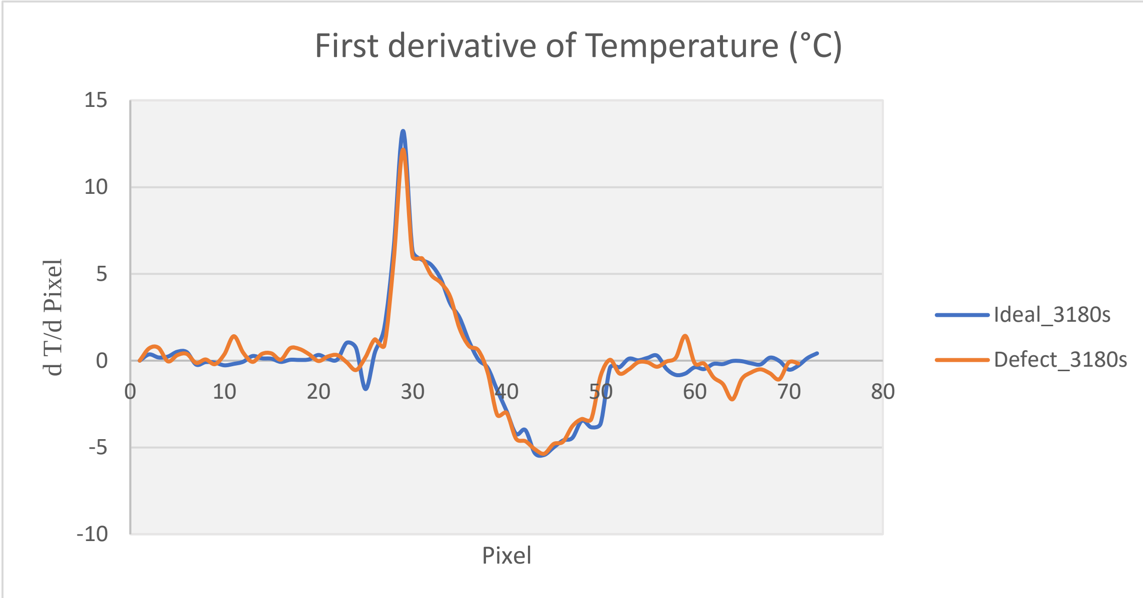

Figure 47: First derivative of temperature with respect to pixel taken at 3180s

For further analysis, the derivative of temperature was taken with respect to the camera pixel, $\frac{dT}{dP}$, to examine where the defect location was. Comparing the results of this with the ideal specimen and the defective specimen, it can be seen that there was a noticeable increase followed by a sudden decrease in $\frac{dT}{dP}$ around pixel 60 indicating a defect along the length of the sample. The drastic increase and decrease of $\frac{dT}{dP}$ from pixel 25 to 50 can be attributed to the vast temperature of the heating pad. The positive peak around pixel 60 can be attributed to the temperature increase before the defect, while the negative peak seen around pixel 65 can be attributed to the decrease in temperature after the defect due to the lack of heat flowing through the defect. By analyzing this response and taking into consideration the temperature differential across the location of the defect, it is obvious there is a lack of heat transferring at this location indicating a defect is present.

CHAPTER 7: CONCLUSIONS

7.1 COMPLETED WORK

Through the research performed, a cost-effective TNDT trainer was developed to provide on-campus and distance learning students experience with a NDT method using active thermography. Each component was carefully chosen to keep costs down making it possible to replicate this trainer so that multiple trainers would be available to a classroom for on-campus students. The trainer used a Raspberry Pi with a unique IP address making it possible for experiments to be performed by distance learning students using virtual reservations.

The process in choosing the material of the test specimen and defect dimensions was verified through simulations and measured results. Simulations provided useful insight in which material should be chosen based off its thermal properties. Aluminum was the best choice for the material because of its high thermal conductivity resulting in a quick thermal response to the heat source. Various defect dimensions were simulated to choose a defect forcing students to use various analysis methods to determine which sample is defective and where the defect may lie. Measured results verified the thermal response of the simulations. It is important to point out that simulations did differ from measured results in two different ways. The first being the time it takes for the specimen to heat up and reach steady-state. The second noticeable difference was the temperatures measured along the specimen when heat was applied from the heating pad. Both of these variances may be due to parameters assumed in conductive and convective heat transfer elements used in simulations.

Careful consideration was taken when creating a conversion equation to convert raw pixel data from the FLIR Lepton module to useful temperature data. The IR broadband pyrometer was used as an accurate method to measure known temperatures to compare the temperature to relate to raw pixel data. The specifications of the camera verified the accuracy of the broadband pyrometer and showed a similar IR wavelength range (8μm - 13μm) compared to that of the FLIR Lepton module (8μm - 14μm). Multiple equations were tested to obtain the best conversion method. The average %Error was calculated for each conversion equation using three different images of a hand at 6”, 12”, and 18” away. A total of 72 different test points were used to compare the measured temperature to calculated temperatures using the conversion equations. The conversion equation with the lowest average %Error across the 72 different test points was selected and implemented in image processing code.

Image processing techniques were applied using MATLAB software to provide multiple useful forms of feedback so students could analyze each thermal image to make a decision whether or not a test subject is defective or not. Among these forms of feedback are thermal images in the form of a 60x80 array consisting of temperatures, thermal images with a custom colormap and temperature data at each pixel location, and temperature graphs depicting the thermal response of each test subject.

7.2 FUTURE WORK

While this research focuses on one specific example of a laboratory trainer setup, this could be used for different TNDT applications. The main assembly that actually captures images is the FLIR Lepton module and Raspberry Pi combination. With these two devices integrated, the FLIR Lepton module can capture thermal images while the Raspberry Pi is able to retrieve and save these images for further processing. Because of this, a different test may be setup for the FLIR Lepton module to capture images of. For example, TNDT may be extremely useful in troubleshooting circuit boards with failed components. The same principle used for this experiment may be applied to one similar using a circuit board. Students may test two circuit boards for proper functionality. Once power is cycled on to these boards, the thermal imaging module would capture images at various time steps to determine if the board is good or not. Similar processing techniques may be implemented using MATLAB and useful feedback for students would be provided. This application and others will be explored with the overall goal of introducing students to an effective NDT method for testing equipment.

REFERENCES

[1] J. Ma and J. V. Nickerson, “Hands-on, Simulated, and Remote Laboratories: A Comparative Literature Review,” *ACM Comput Surv*, vol. 38, no. 3, Sep. 2006.

[2] H. Ewald, “Experiments by Remote Control Using the Internet,” *ResearchGate*.

[3] B. Alhalabi, M. K. Hamza, and A. A.-E. Humos, “Distance Education: Remote Labs Environment,” *Am. Soc. Eng. Educ.*

[4] “What is NDT? | Nondestructive Testing School.” [Online]. Available: http://www.trainingndt.com/what-is-nondestructive-testing. [Accessed: 01-Mar-2017].

[5] “Thermal NDT: Historical milestones, state-of-the-art and trends (PDF Download Available),” *ResearchGate*. [Online]. Available: https://www.researchgate.net/publication/263764848_Thermal_NDT_Historical_milestones_state-of-the-art_and_trends. [Accessed: 10-Mar-2017].

[6] “A comparison of hands-on versus remote laboratory experience for introductory microprocessors courses,” *ResearchGate*.

[7] I. Colak and A. Efe, “Design and implementation of a remote access PLC training set,” in *International Aegean Conference on Electrical Machines and Power Electronics and Electromotion, Joint Conference*, 2011, pp. 425–429.

[8] A. F. Browne and D. Vutetakis, “Innovative approach for dual control of electromechanical plant,” in *SoutheastCon 2015*, 2015, pp. 1–4.

[9] A. F. Browne, W. B. Williams, K. Loftus, and C. Nye, “Implementation of a Cartesian robot for remote Mission Critical Operator training,” in *SoutheastCon 2016*, 2016, pp. 1–4.

[10] “Application of infrared thermography to the non-destructive testing of concrete and masonry bridges (PDF Download Available),” *ResearchGate*.

[11] J. A. Schroeder, T. Ahmed, B. Chaudhry, and S. Shepard, “Non-destructive testing of structural composites and adhesively bonded composite joints: pulsed thermography,” *Compos. Part Appl. Sci. Manuf.*, vol. 33, no. 11, pp. 1511–1517, Nov. 2002.

[12] N. P. Avdelidis, C. Ibarra-Castanedo, and X. P. V. Maldague, “Infrared thermography inspection of glass reinforced plastic (GRP) wind turbine blades and the concept of an automated scanning device,” 2013, vol. 8705, p. 87050G–87050G–6.

[13] “Introduction to NDT by active infrared thermography,” *ResearchGate*.

[14] FLIR, “FLIR Lepton Long Wave Infrared (LWIR) Datasheet.” 15-Oct-2014.

[15] “Solid Statements Newsletters | Crydom.” [Online]. Available: http://www.crydom.com/en/tech/newsletters.shtml. [Accessed: 02-Mar-2017].

[16] “FLiR Dev Kit - KIT-13233 - SparkFun Electronics.” [Online]. Available: https://www.sparkfun.com/products/13233. [Accessed: 07-May-2017].

APPENDIX A: FLIR LEPTON CAMERA

FLIR LEPTON® Long Wave Infrared (LWIR) Datasheet

General Description

Lepton® is a complete long-wave infrared (LWIR) camera module designed to interface easily into native mobile-device interfaces and other consumer electronics. It captures infrared radiation input in its nominal response wavelength band (from 8 to 14 microns) and outputs a uniform thermal image.

Features

- Dimensions:

  8.5 x 11.7 x 5.6 mm (without socket),
  10.6 x 11.7 x 5.9 mm (including socket)

- 51-deg HFOV, 63.5-deg diagonal (f/1.1 silicon doublet)
- LWIR sensor, wavelength 8 to 14 μm
- 80 (h) × 60 (v) active pixels
- Thermal sensitivity <50 mK
- Integrated digital thermal image processing functions, including automatic thermal environment compensation, noise filters, non-uniformity correction, and gain control
- Optional temperature-stable output to support radiometric processing
- Export compliant frame rate (< 9 Hz)
- MIPI and SPI video interfaces
- Two-wire I2C-like serial-control interface
- Uses standard cell-phone-compatible power supplies: 2.8V to sensor, 1.2V to digital core, and flexible IO from 2.5V to 3.1V
- Fast time to image (< 0.5 sec)

- Low operating power, nominally 150 mW (< 160 mW over full temperature range)
- Low power standby mode
- RoHS compliant
- 32-pin socket interface to standard Molex or similar side-contact connector

Applications

- Mobile phones
- Gesture recognition
- Building automation
- Thermal imaging
- Night vision

APPENDIX B: OMEGA FLEXIBLE SILICONE RUBBER FIBERGLASS INSULATED HEATER SPECIFICATIONS

FLEXIBLE HEATERS OMEGA®

FLEXIBLE SILICONE RUBBER FIBERGLASS INSULATED HEATERS

SRF Series

- Lightweight Thin, Flexible
- Available in 2.5, 5 and 10 W/in²
- -56 to 232°C (-70 to 450°F) Operating Temperature
- Etched Foil and Wire Wound Design
- Round or Rectangular Shapes
- Available in 115 or 230** Vac
- Optional Pressure Sensitive Adhesive (PSA)†

1 YEAR WARRANTY

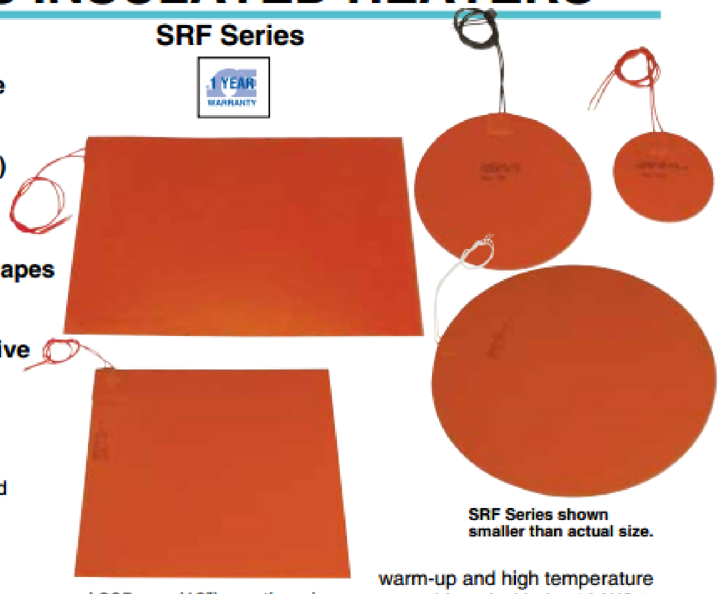

SRF Series shown smaller than actual size.

OMEGALUX® silicone rubber fiberglass insulated flexible heaters can improve heat transfer and speed warm-ups where controlled heating is required in confined areas. Two circuit designs are available: etched foil or wire wound. Heaters with etched foil designed elements are available where the length or width dimension is less than 305 mm (12"). All other heaters where both the length and the width dimensions exceed 305 mm (12") use the wire-wound element design. Effect of power density: gentle warming is best done with 2.5 W/in². A good all purpose unit is the 5 W/in². Rapid warm-up and high temperature are achieved with the 10 W/in²; however, temperature must be controlled as the safe maximum operating temperature limit of 232°C (450°F) may be exceeded.

Round Silicone Rubber Heaters

To Order

Diameter	Total Wattage for Watt Density			Without PSA	With PSA
cm (inch)	2.5 W/in²	5 W/in²	10 W/in²	Model No.	Model No.
7.6 (3)	17.5	35	70	SRFR-3/*	SRFR-3/*-P
10 (4)	31.4	62.8	125.6	SRFR-4/*	SRFR-4/*-P
13 (5)	49.0	98.15	196.3	SRFR-5/*	SRFR-5/*-P
15 (6)	70.67	141.3	282.7	SRFR-6/*	SRFR-6/*-P
18 (7)	96.2	192.4	384.8	SRFR-7/*	SRFR-7/*-P
20 (8)	125.65	251.3	502.6	SRFR-8/*	SRFR-8/*-P
23 (9)	157.9	315.8	631.7	SRFR-9/*	SRFR-9/*-P
25 (10)	196.25	392.5	785	SRFR-10/*	SRFR-10/*-P
28 (11)	237.45	474.9	949.8	SRFR-11/*	SRFR-11/*-P
30 (12)	376.8	753.6	1507.2	SRFR-12/*	SRFR-12/*-P

Comes complete with operator's manual

** Insert watt density: 2 for 2.5 W/in², 5 for 5 W/in² or 10 for 10 W/in².*

*** Most sizes available in 230V. Contact Engineering.*

† Heaters with pressure sensitive adhesive: max operating temperature is 149°C (300°F).

***Ordering Examples: SRFR-3/10**, 7.6 cm (3") diameter heater with a watt density of 10 W/in² and 70 watts of total power.*

***SRFR-11/10**, 28 cm (11") diameter heater with a 10 W/in², 949 watts.*

CAUTION AND WARNING!
Fire and electrical shock may result if products are used improperly or installed or used by non-qualified personnel. See inside back cover for additional warning.

Rectangular Silicone Rubber Heaters

To Order

Width, cm (")	Length, cm (")	Total Wattage for Watt Density 2.5 W/in²	5 W/in²	10 W/in²	Without PSA Model No.	With PSA Model No.
2.5 (1)	2.5 (1)	–	–	10	**SRFG-101/10**	**SRFG-101/10-P**
2.5 (1)	5 (2)	5	10	–	**SRFG-102/***	**SRFG-102/*-P**
2.5 (1)	7.6 (3)	7.5	15	30	**SRFG-103/***	**SRFG-103/*-P**
2.5 (1)	10 (4)	10	20	40	**SRFG-104/***	**SRFG-104/*-P**
2.5 (1)	13 (5)	12.5	25	50	**SRFG-105/***	**SRFG-105/*-P**
2.5 (1)	15 (6)	15	30	60	**SRFG-106/***	**SRFG-106/*-P**
2.5 (1)	18 (7)	17.5	35	70	**SRFG-107/***	**SRFG-107/*-P**
2.5 (1)	20 (8)	20	40	80	**SRFG-108/***	**SRFG-108/*-P**
2.5 (1)	23 (9)	22.5	45	90	**SRFG-109/***	**SRFG-109/*-P**
2.5 (1)	25 (10)	25	50	100	**SRFG-110/***	**SRFG-110/*-P**
2.5 (1)	28 (11)	27.5	55	110	**SRFG-111/***	**SRFG-111/*-P**
2.5 (1)	30 (12)	30	60	120	**SRFG-112/***	**SRFG-112/*-P**
2.5 (1)	46 (18)	45	90	180	**SRFG-118/***	**SRFG-118/*-P**

Comes complete with operator's manual.
** Insert watt density: 2 for 2.5 W/in², 5 for 5 W/in² or 10 for 10W/in².*
*** Most sizes available in 230V. Consult heater sales and engineering.*

Ordering Example: SRFG-712/5-P, *18 x 30 cm (7 x 12") heater with a watt density of 5 W/in², total rated wattage output of 420 watts, with optional pressure sensitive adhesive.*

Note: *Heaters are available in only the watt densities where total wattage is shown. Heaters with pressure sensitive adhesive: max operating temperature is 149°C (300°F).*

APPLICATIONS

- **Freeze Protection**
- **Low Temperature Ovens**
- **Heat Tracing Systems**
- **Viscosity Control**
- **Dehumidification of Motors and Control Devices**

SPECIFICATIONS

Wattage: 5 to 1440 Watts
Power: 115 or 230** Vac
Watt Density: 2.5, 5 and 10 W/in²
Lead Wire: 305 mm (12") PFA insulated
Thickness: 0.030 to 0.070", except at lead wire exit
Dielectric Strength: 1250 Vac
Maximum Temperature: heaters without pressure sensitive adhesive, 232°C (450°F); heaters with pressure sensitive adhesive, 149°C (300°F)
Minimum Temperature: -56°C (-70°F)

APPENDIX C: SOLID-STATE RELAY

FOTEK **SSR SERIES** DC TO AC SOLID STATE RELAY c UL us CE

Specification

Type	Terminal Type					PCB Type
Model	**SSR-10DA**	**SSR-25DA**	**SSR-40DA**	**SSR-25DA-H**	**SSR-40DA-H**	**SSR-P03DA**
Rated Load Current	**10A**	**25A**	**40A**	**25A**	**40A**	**3A**
Input Data						
Operating Voltage	3~32VDC					
Min. ON / OFF Voltage	ON > 2.4V , OFF < 1.0V					
Trigger Current	7.5mA / 12V					
Control Method	Zero Cross Trigger					
Output Data						
Operating Voltage	24~380VAC			90~480VAC		24~380VAC
Min. Black Voltage	600 VAC < Repetive >					
Voltage Drop	1.6 V / 25 C					
Max. Durated Current	135A	275A	410A	275A	410A	135A
Leakage Current	3.0mA	3.0mA	3.0mA	5.0mA	5.0mA	3.0mA
Response Time	ON < 10ms , OFF < 10ms					
General Data						
Dielectric Strength	Over 2.5KVAC / 1min.					
Isolation Strength	Over 50MΩ / 500VDC					
Operating Temperature	-20 C ~+80 C					
Housing Material	Intensive ABS					
Weight	Appr. 105g					Appr. 15g

FOTEK SSR SERIES HIGH CURRENT DC TO AC SOLID STATE RELAY

Specification

Type	Terminal Type			
Model	SSR-50DA	SSR-75DA	SSR-50DA-H	SSR-75DA-H
Rated Load Current	50A	75A	50A	75A
Input Data				
Operating Voltage	3~32VDC			
Min. ON / OFF Voltage	ON>2.4V , OFF<1.0V			
Trigger Current	7.5mA / 12V			
Control Method	Zero Cross Trigger			
Operating Data				
Operating Voltage	24~380VAC		90~480VAC	
Min. Blocking Voltage	600 VAC<Repetitive>			
Voltage Drop	1.6V / 25℃			
Max. Duratde Current	550A	820A	550A	820A
Leakage Current Max.	6.0mA	6.0mA	6.0mA	6.0mA
Response Time	ON<10ms , OFF<10ms			
General Data				
Dielectric Strength	Over 2.5KVAC/1min.			
Isolation Strength	Over 50M Ω/ 500VDC			
Operating Temperature	-20℃ ~+80℃			
Housing Material	Intensive ABS			
Weight	Appr.125g			

Connection Diagram/Dimension

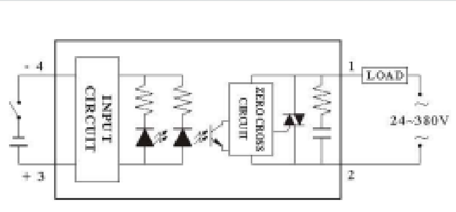

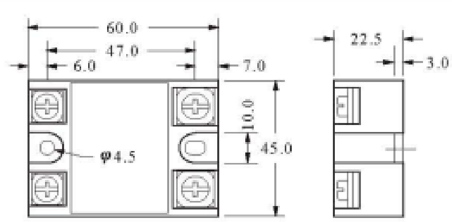

APPENDIX D: SIMULINK SIMULATION MODEL IMAGES

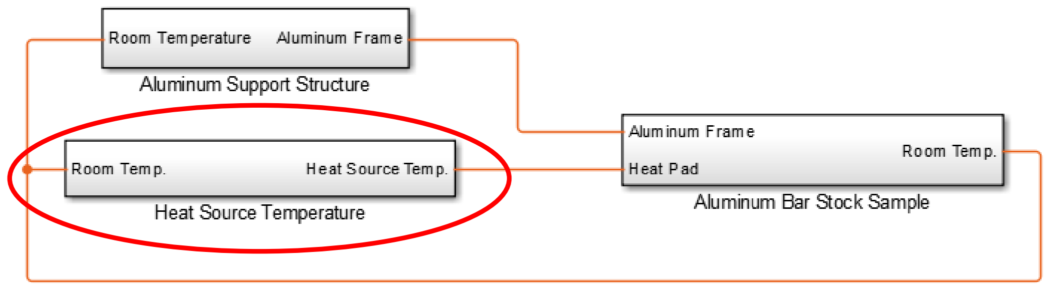

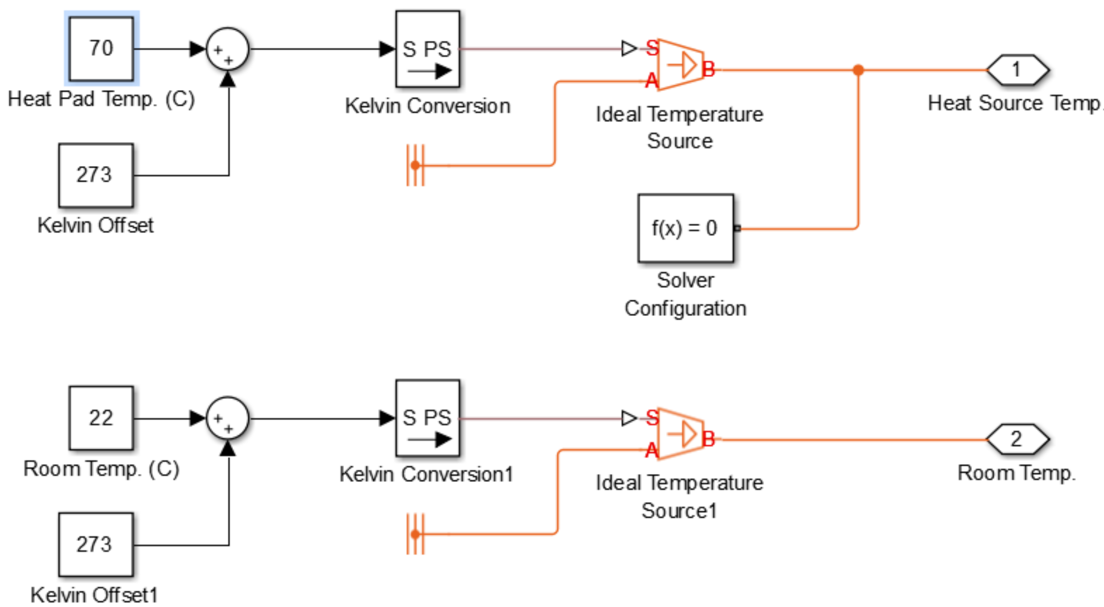

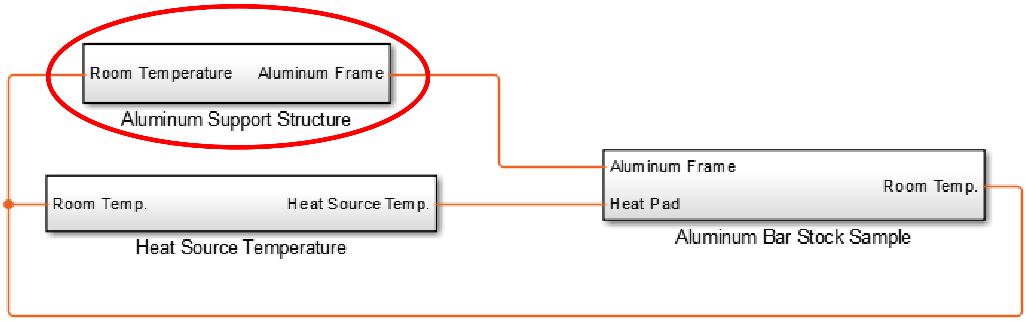
Room Temperature
Aluminum Frame
Aluminum Support Structure
Room Temp.
Heat Source Temp.
Heat Source Temperature
Aluminum Frame
Room Temp.
Heat Pad
Aluminum Bar Stock Sample

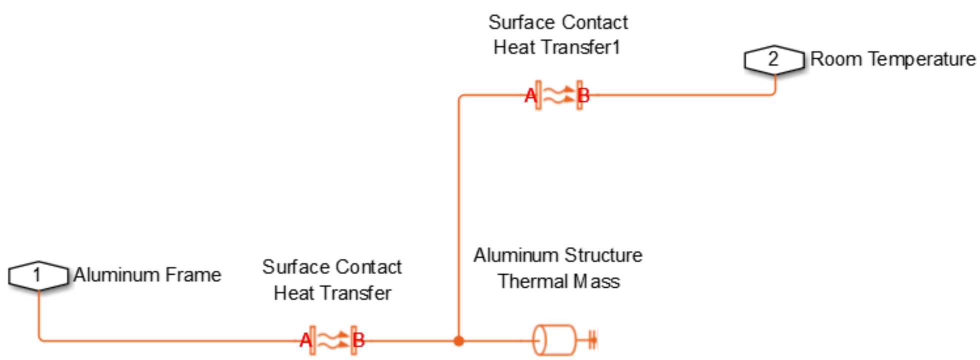
Surface Contact
Heat Transfer1
2
Room Temperature
1
Aluminum Frame
Surface Contact
Heat Transfer
Aluminum Structure
Thermal Mass
A
B
A
B

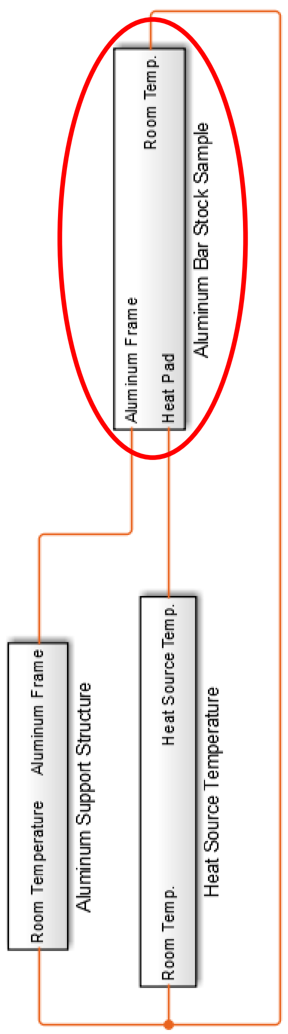
Room Temperature
Aluminum Frame
Aluminum Support Structure
Room Temp.
Heat Source Temp.
Heat Source Temperature
Aluminum Frame
Heat Pad
Room Temp.
Aluminum Bar Stock Sample

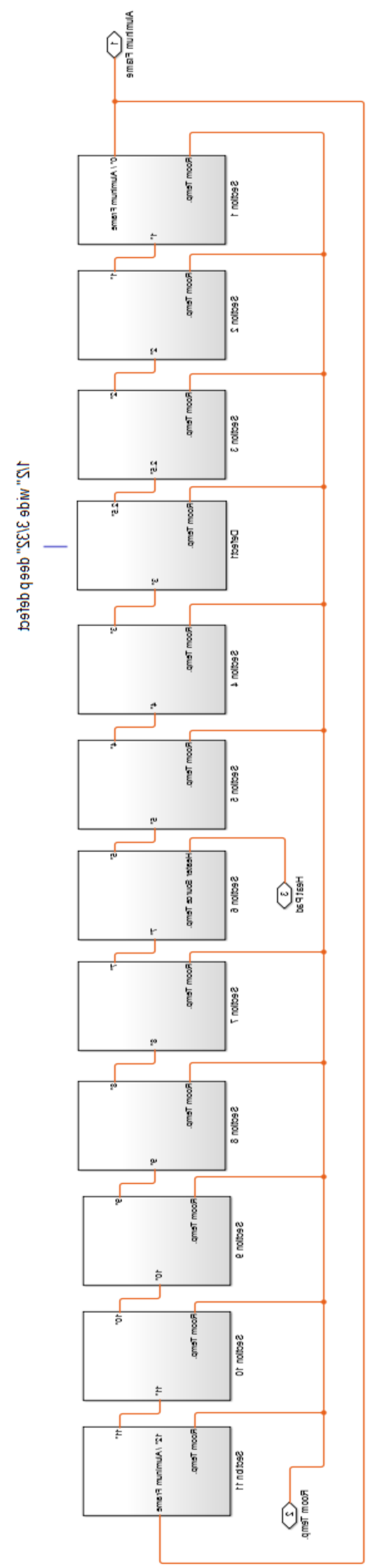
1/2" wide 3/32" deep defect

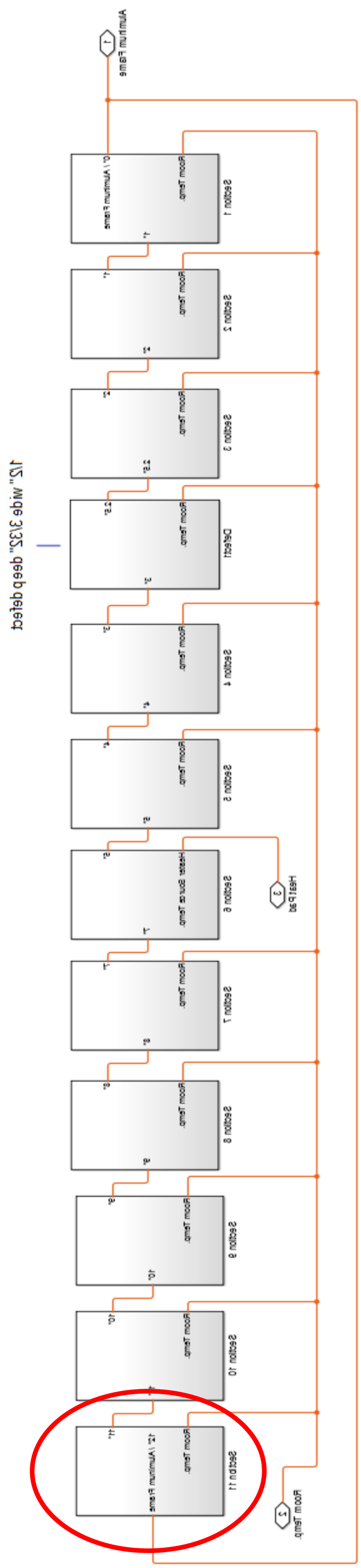

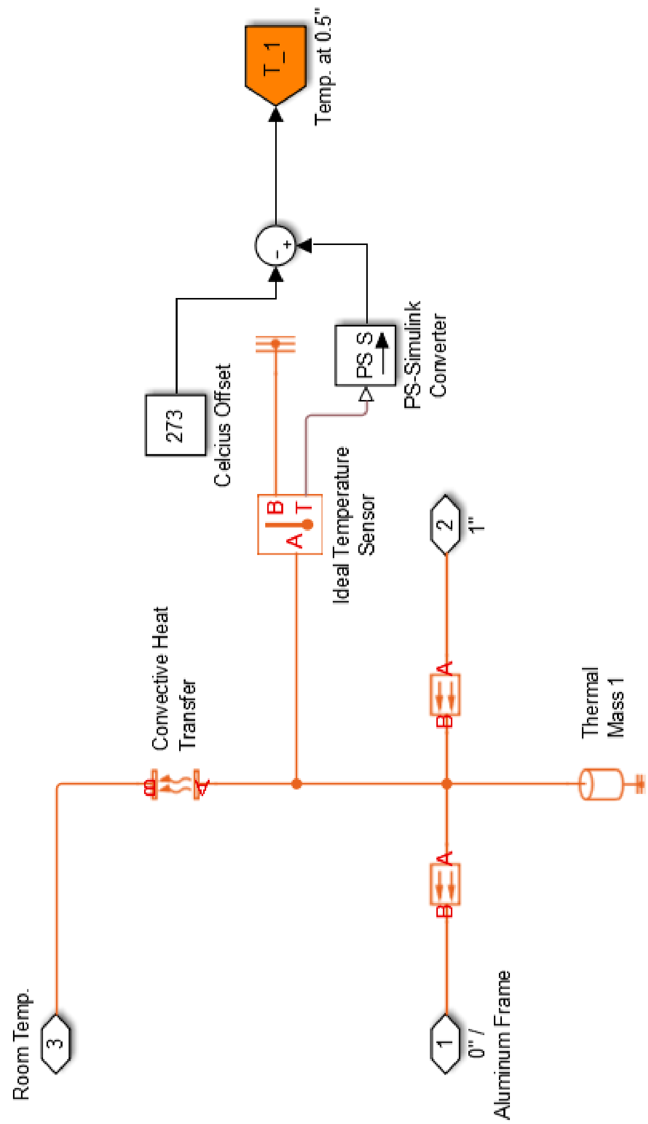
Room Temp.
3
Convective Heat Transfer
Ideal Temperature Sensor
273
Celcius Offset
PS-Simulink Converter
T_1
Temp. at 0.5"
2
1"
Thermal Mass 1
1
0" / Aluminum Frame